

# Back-scattering correction and further extensions of Amiet's trailing-edge noise model. Part II: Application

Stéphane Moreau<sup>a,\*</sup>, Michel Roger<sup>b</sup>

<sup>a</sup>*Engine Cooling Fan Systems Core Competencies Group, Valeo Engine Cooling, 78321 La Verrière, France*

<sup>b</sup>*Laboratoire de Mécanique des Fluides et Acoustique, Ecole Centrale de Lyon, 69134 Ecully, France*

Received 9 December 2007; received in revised form 19 November 2008; accepted 20 November 2008

Handling Editor: C.L. Morfey

Available online 30 January 2009

---

## Abstract

The analytical model of the trailing-edge noise of an airfoil derived in the first part of this study is assessed by first comparing the predictions with alternative analytical and numerical computations found in the literature. Comparisons are also made with experimental data. The data are either taken from the literature or collected in a series of new experiments run in open-jet anechoic wind tunnels. Several configurations have been investigated, ranging from a flat plate to symmetric and cambered, thick and thin airfoils, at various angles of attack triggering various flow regimes at different Reynolds numbers. The comparisons address the distribution of the far-field radiated noise both in frequency and radiation angle. The transfer function between the wall-pressure fluctuations in the vicinity of the trailing edge and the noise radiated in the far field is found experimentally to be roughly independent of the flow conditions encountered on the airfoil, as far as the mean flow remains attached. The good agreement of the present predictions with both the measurements and the alternative theories not only emphasises the relevance and accuracy of the model but also stresses the effect of the finite chord length in the noise generation and radiation mechanisms. Moderate airfoil camber and angle of attack are shown to be of secondary importance on the noise radiation, even though they fully determine the sources of the noise through the flow field. All comparisons make the model accurate enough provided precise flow data are available. © 2009 Elsevier Ltd. All rights reserved.

---

## 1. Introduction

In the design of a new fan, such as the ones used in automotive engine cooling systems, one major specification that is to be fulfilled is a minimum noise configuration for several operating conditions. As mentioned in Ref. [1], the noise is the sum of discrete tones associated with the periodic part of the blade loads and a broadband spectrum associated with the random loads due to the turbulence in the flow, both contributions being roughly of equal weight in most cases. The broadband noise can even be more important, or dominant, in other low-speed axial fans such as the propellers of air conditioning units, or in the large wind turbines. Various generating mechanisms have been identified for the broadband noise [2]. The impingement of the wakes shed by the rotor blades on downstream obstacles (e.g. stator vanes) first contributes.

---

\*Corresponding author. Tel.: +33 1 30 13 51 55; fax: +33 1 30 13 54 70.

E-mail address: [stephane.moreau@valeo.com](mailto:stephane.moreau@valeo.com) (S. Moreau).

<b>Nomenclature</b>	
$AR$	acoustic pressure PSD ratio
$b_c$	Corcos non-dimensional parameter
$c = 2b$	airfoil chord length
$c_0$	sound speed in quiescent medium
$e$	flat plate thickness
$f_0$	flat plate characteristic frequency of von Karman vortex street
$\mathcal{I}$	radiation integral
$k$	acoustic wavenumber
$K_1, K_2$	streamwise and spanwise aerodynamic wavenumbers
$l_y$	spanwise correlation length
$L$	airfoil span length
$M_0, M_{0r}$	absolute and relative free-stream Mach number
$M_c, M_{cr}$	absolute and relative Mach number based on boundary-layer convection velocity
$M_w, M_{wr}$	absolute and relative Mach number based on wake convection velocity
$P_0, P_1$	incident and scattered pressure
$S_0$	corrected distance for convection effects
$S_{pp}$	far-field acoustic PSD
$U_0$	free-stream velocity
$U_c$	boundary-layer convection velocity
	$W$ wake convection velocity
	$\vec{x} = (x_1, x_2, x_3)$ observer cartesian coordinate system
	$(R, \psi, \theta)$ experimental coordinate system
	$(R, \alpha, \theta)$ Amiet's coordinate system
	$(R, \bar{\alpha}, \bar{\theta})$ Howe's coordinate system
	$(R_e, 0, \theta_e)$ emission coordinate system in the mid-span plane
	$\alpha_g$ geometrical angle of attack
	$\beta$ compressibility parameter
	$\Lambda, \Lambda^*$ dimensionless radiation ratios
	$\mu$ frequency parameter
	$\Pi_0$ streamwise integrated wavenumber spectral density of wall-pressure fluctuations
	$\Phi_{pp}$ wall-pressure PSD
	$\omega$ angular frequency
	<i>Superscripts</i>
	$(\bar{\cdot})$ made non-dimensional by $b$
	$(\cdot)^A$ Amiet's formulation
	$(\cdot)^H$ Howe's formulation
	$(\cdot)^\infty$ limit value for arbitrary large aspect ratio
	$(\cdot)_e$ Emission coordinates

The vortical structures in the recirculating flow in the tip clearance also contribute as more localised sources. Then a possible amount of upstream turbulence at inlet interacts with the rotor blades, yielding the turbulence-interaction noise, the sources of which concentrate at the leading edge. Finally, broadband noise is generated as the vorticity in the fluctuating boundary layers on the blades is scattered at the trailing edge into acoustic waves. This mechanism is called trailing-edge noise and provides the minimum noise that the spinning fan would produce free of any upstream, downstream and tip interactions [3]. Moreover, if the boundary-layer thickness is small enough when compared to the thickness of the trailing edge, a von Kármán vortex street occurs in the wake, leading to an additional narrow-band vortex-shedding noise. This mechanism also radiates preferentially from the trailing edge but is considered as different of the pure trailing-edge noise.

If the blade spacing to chord length ratio is relatively large, turbulence-interaction noise and trailing-edge noise can be modelled with an expected reasonable accuracy by means of analytical formulae based on a single-airfoil approach [4]. The key point is a transfer function relating in each case the aerodynamic wall-pressure statistics [5,6] or the incoming velocity statistics [7] to the far-field pressure power spectral density (PSD). In the first part of this study [8], a detailed extension of Amiet's original work [5,7] has been derived that provides the trailing-edge noise of an isolated airfoil from a statistical description of the wall-pressure field near the trailing edge. The model accounts for the finite chord length of the airfoil by adding a leading-edge back-scattering correction to the main turbulence scattering at the trailing edge. The fluctuations are split into general three-dimensional oblique gusts, necessary for a proper assessment of the sound radiated off the mid-span plane and that of the effect of a finite aspect ratio. The model ignores the detailed geometry (blade camber, thickness and exact trailing-edge shape), which is indirectly accounted for through the wall-pressure statistics used as input data.

This second part is essentially devoted to the comparison with existing alternative analytical approaches or numerical results on the one hand, and to a detailed assessment against experimental data on the other hand. Furthermore, the present predictions from Ref. [8] are compared all along the paper to their asymptotic values for high Helmholtz number  $kc$ , that are shown to be identical to the half-plane model (arbitrary large chord length) derived by Howe [9,10]. The latter model has been extensively used in the literature on trailing-edge noise and, as such, will serve as a reference for the present analysis. The analytical model of part I and Howe’s asymptotic theory are reminded first in Section 2. Section 3 then describes the experimental protocol used to test the theoretical predictions. The first validation step is achieved in Section 4 by checking the predicted directivity patterns at given fixed frequencies against alternative theoretical results and a dedicated experiment. This point is made independently of the flow conditions. The next step, Section 5, is the investigation of the noise spectrum at a given radiation angle. Since this point is strongly flow-dependent, dedicated experiments are performed with various airfoils and different flow conditions. Some existing literature on trailing-edge noise measurements is also used to assess the model. The aforementioned transfer function is effectively found to be nearly invariant.

**2. Analytical formulations**

Some of the trailing-edge noise studies made in the seventies are based on the assumption of a rigid half-plane [9,11] arguing that the scattering process is localised close to the trailing edge and is nearly independent of what happens farther upstream. However, this assumption provides only an asymptotic trend, the actual chord length being of primary importance when assessing the far-field sound directivity. That is why the chord length was explicitly accounted for in Amiet’s formulation [5] and more completely in its extension described in the first part of this paper [8]. An alternative approach suited to a finite chord and a vanishingly low Mach number has also been proposed recently by Howe [14]. This latter work will be found to be identical to a low-Mach number application of the present model in the next subsections, and will not be addressed later on in the paper. In the present study, the main focus is the solution derived in part I [8]. Howe’s asymptotic theory [9] is used to compare the finite-chord results against the well documented half-plane results.

*2.1. Howe’s and extended Amiet’s models*

As shown in part I, the far-field acoustic pressure PSD of a flat rectangular airfoil of arbitrary span  $L$  and chord length  $c$  can be written as

$$S_{pp}(\vec{x}, \omega) = \left(\frac{kcx_3L}{4\pi S_0^2}\right)^2 \frac{2}{c} \int_{-\infty}^{\infty} \Pi_0^A(\omega, \vec{K}_2) \text{sinc}^2\left\{\frac{L}{c}\left(\vec{K}_2 - k\frac{x_2}{S_0}\right)\right\} \left|\mathcal{I}\left(\frac{\vec{\omega}}{U_c}, \vec{K}_2\right)\right|^2 d\vec{K}_2 \tag{1}$$

where the notation  $\text{sinc}(\xi)$  stands for the function  $\sin(\xi)/\xi$ , and the corresponding asymptotic result in the case of a very large aspect ratio  $L/c \rightarrow \infty$  reads

$$S_{pp}(\vec{x}, \omega) = \left(\frac{kcx_3}{4\pi S_0^2}\right)^2 2\pi L \left|\mathcal{I}\left(\frac{\omega}{U_c}, k\frac{x_2}{S_0}\right)\right|^2 \Pi_0^A\left(\omega, k\frac{x_2}{S_0}\right) \tag{2}$$

Eqs. (1) and (2) have three main terms: the radiation integral  $\mathcal{I}$  given in Ref. [8], the wall-pressure wavenumber spectral density  $\Pi_0^A$  and a directivity factor including the dipole-like ratio  $(x_3/S_0^2)^2$ .  $\vec{K}_2 = K_2c/2$  is a dimensionless aerodynamic wavenumber in the spanwise direction. Other notations are found in the nomenclature or defined later on. The coordinate system is described in Fig. 1. Furthermore

$$\Pi_0^A\left(\omega, k\frac{x_2}{S_0}\right) = \frac{1}{\pi} \Phi_{pp}(\omega) \ell_y\left(k\frac{x_2}{S_0}, \omega\right) \tag{3}$$

where  $\Phi_{pp}$  is the aerodynamic wall-pressure spectrum, taken in the close vicinity of the trailing edge but far enough upstream for the information to correspond only to the incident pressure field of the boundary-layer turbulence, free of edge scattering.  $\ell_y$  is the associated spanwise correlation length.

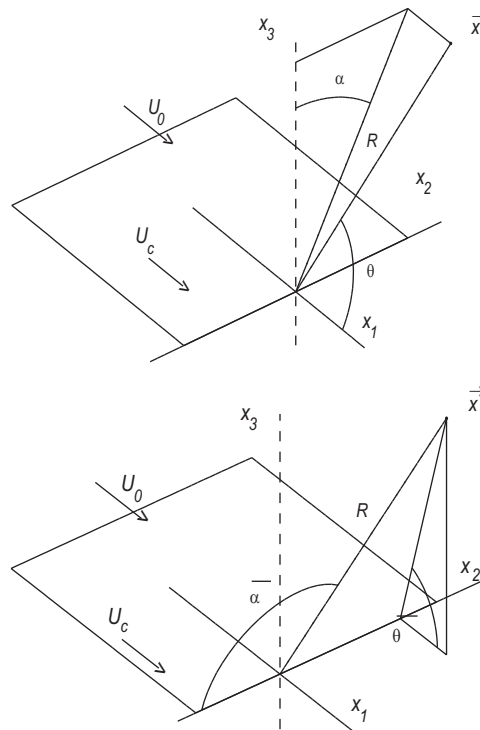


Fig. 1. Reference frames at a trailing edge used in Amiets’s model (top) and Howe’s asymptotic model (bottom).

The solution holds for a stationary airfoil and a stationary observer, the ambient fluid moving with the uniform speed  $U_0$  in the  $x_1$  direction.  $S_0$  is a corrected distance accounting for the convection of the acoustic waves by the flow

$$S_0 = x_1^2 + \beta^2(x_2^2 + x_3^2) \quad \text{with } \beta^2 = 1 - M_0^2, \quad M_0 = U_0/c_0$$

According to Howe’s asymptotic theory [9,15], the alternative expression, assuming the same full Kutta condition as for Eq. (2), can be written as (Eq. (72) of Ref. [9])

$$S_{pp}^H(\vec{x}, \omega) = \frac{M_c L \sin \bar{\alpha} \sin^2(\bar{\theta}/2) \Pi_0^H(\omega, k \cos \bar{\alpha})}{\pi R^2 (1 + M_{0r})^2 (1 - M_{cr})^2 (1 - M_{wr})^2 (1 - M_c \sin \bar{\alpha})} \quad (4)$$

where  $M_{0r} = M_0 x_1/R$ ,  $M_{cr} = M_c x_1/R$ ,  $M_{wr} = M_w x_1/R$  are relative Mach numbers in the direction of the observer.  $M_c = U_c/c_0$  and  $M_w = W/c_0$  are the Mach numbers based on the convection speeds of the disturbances  $U_c$  and  $W$ , in the boundary layer and in the wake, respectively. Typical values proposed by Howe and used in the following numerical tests are  $U_c = 0.7U_0$  and  $W = 0.5U_0$ . This point may be controversial when the equation is checked against measured data. The true turbulent field in the boundary layers and in the wake does not correspond to a constant convection speed. Furthermore, according to Brooks and Hodgson [15], no experimental evidence is found of a secondary vorticity in the wake at a speed  $W$ , and it can be assumed that eddies formed close to the trailing edge have a negligible initial speed before being accelerated in the wake. For that reason, Brooks and Hodgson propose to simply put  $W = 0$  in Howe’s model for a best fit with the measurements. Note also that a factor 2 has been suppressed in Eq. (4) with respect to Howe’s original result, as again proposed by Brooks and Hodgson [15]. This allows to consider  $\Pi_0^H$  as the wall-pressure statistics effectively taken at some distance upstream, instead of in the very vicinity, of the trailing edge. Indeed, Howe’s analysis explicitly includes the effect of vortical eddies from the boundary layer and from the wake. The corresponding wall-pressure statistics must account for both, which means that it must be evaluated quite close to the trailing edge, typically at an upstream distance smaller than a characteristic eddy size. In Amiet’s approach, the wall-pressure statistics must only account for the incident boundary-layer

disturbances, irrespective of their modification around the trailing edge. It must be evaluated at a point significantly farther upstream. However, this approach holds if the aerodynamic wall-pressure field remains almost homogeneous between that point and the trailing edge. This will be checked in Section 5.2. Brooks and Hodgson's hypothesis  $W = 0$  with regard to Howe's model is equivalent to the pressure release imposed at the trailing edge in the extended Amiet's model of part I. As a consequence,  $\Pi_0^H$  and  $\Pi_0^A$  must be understood as the same input data when  $W = 0$ .

Eq. (4) is based on another set of coordinates also shown in Fig. 1 and defined by the following relationships:

$$\begin{cases} x_1 = R \sin \bar{\alpha} \cos \bar{\theta} = R \cos \theta \\ x_2 = R \sin \bar{\alpha} \sin \bar{\theta} = R \sin \theta \cos \alpha \\ x_3 = R \cos \bar{\alpha} = R \sin \theta \sin \alpha \end{cases} \quad (5)$$

Thus

$$\sin \bar{\alpha} \cos \bar{\theta} = \cos \theta, \quad \sin \bar{\alpha} = \sqrt{1 - \sin^2 \theta \sin^2 \alpha}, \quad \cos \bar{\alpha} = \sin \theta \sin \alpha$$

In the mid-span plane ( $\alpha = 0, \bar{\alpha} = \pi/2$ ),  $\bar{\theta}$  becomes identical to  $\theta$ . The solutions will be specified in that plane from now on.

As shown in Appendix A, the low Mach number approximations of Amiet's and Howe's formulae read

$$S_{pp}^A(\vec{x}, \omega) \simeq \left(\frac{kc}{2\pi}\right)^2 \frac{\sin^2 \theta L}{R^2} \frac{1}{2} |\mathcal{S}|^2 \Phi_{pp}(\omega) l_y(\omega) \quad (6)$$

and

$$S_{pp}^H(\vec{x}, \omega) \simeq \left(\frac{\sqrt{2}}{\pi}\right)^2 \frac{L}{2} \frac{\sin^2(\theta/2) M_c \Phi_{pp}(\omega) l_y(\omega)}{R^2 (1 - M_c) [1 + 2(M_0 - M_c - M_w) \cos \theta]} \quad (7)$$

respectively. At both very high frequencies and vanishing Mach numbers ( $M_0 \ll 1$ ), Eqs. (6) and (7) yield

$$S_{pp}^A(\vec{x}, \omega) = S_{pp}^H(\vec{x}, \omega) \simeq \left(\frac{\sqrt{2}}{\pi}\right)^2 \frac{\sin^2(\theta/2) L}{R^2} \frac{1}{2} M_c \Phi_{pp}(\omega) l_y(\omega) \quad (8)$$

Now in the first part of the paper [8], a scattered pressure  $P_1$  equal in amplitude to the incident pressure  $P_0$  is applied with opposite phases on both sides of the airfoil. It yields twice the scattered field predicted by Amiet [5], as shown by comparing Eq. (1) to the reference formula. This may be a point of controversy. Indeed Zhou and Joseph [19] pointed out that the Kutta condition must be imposed on the total pressure difference between the suction side and the pressure side. Therefore, for an incident pressure on one side only,  $P_0$  is the total incident pressure jump and the trace of the scattered pressure  $P_1$  on one side must have half that amplitude at the trailing edge. However the additional factor 2 ensures the equivalence with Eq. (8). One may argue that it is necessary in the formulation in order to account for the Kutta condition in the following sense. It is assumed that an incident vortex in the boundary layer is not fundamentally modified when being convected past the trailing edge and follows a path nearly parallel to the model plate. The global dynamics of the flow remains compatible with the condition of no cross-flow in the near wake only if the secondary vorticity shed from the edge acts in the exact continuation of the image vortex that could be put upstream to account for the presence of the plate. According to this ideal behaviour the pressure along the wake is zero since the image vortex has the opposite circulation of the incident one and it must be continuous and zero in the vicinity of the edge. This continuity is ensured if the scattered pressure is in phase opposition on both sides of both the plate and the wake, on the one hand, and if it cancels the image vortex pressure on the side of the plate opposite to the incident vortex, on the other hand. According to this interpretation, the scattered pressure at the trailing edge in the mathematical problem statement must be exactly  $-P_0$  on the same side as the incriminated incident boundary layer, and the counter-pressure  $+P_0$  on the opposite side balances the image vortex. The difference between this statement and Amiet's original one is that the pressure around the edge is continuous and equal to zero instead of being continuous and equal to  $P_0/2$ . Furthermore, the correction leads to predictions in

overall agreement with many experimental test cases on airfoils, as shown in the subsequent sections, as well as on rotating blades [20]. The original statement would systematically under-predict the radiated sound by 6 dB. For these reasons, Eq. (1) and its limit forms are used as such later on in the paper.

Eqs. (6) and (7) will be used in the paper and tested against experimental data. They suggest that, for the same airfoil chord length and flow speed, the dimensionless ratio

$$A = \frac{R^2 S_{pp}(\vec{x}, \omega)}{L \Phi_{pp}(\omega) \ell_y(\omega)}$$

is invariant with respect to the flow regime involved in the boundary-layer dynamics, except for the slight variation of  $|\mathcal{J}|$  with the convection speed [18]. This will be assessed experimentally in Section 5. In contrast, the PSD ratio  $S_{pp}(\vec{x}, \omega)/\Phi_{pp}(\omega)$  is expected to be flow-dependent. The invariance property *a priori* holds only for attached flows on the aft part of an airfoil, for which a convection speed can be clearly defined in the downstream direction.

## 2.2. Assessment of the analytical extensions

In the first part of the paper [8], Amiet's trailing-edge noise theory was extended to explicitly account for a back-scattering at the leading edge and three-dimensional pressure patterns. The effect of the back-scattering was shown to be theoretically important both at low frequencies or as  $\bar{k}x_2/S_0$  approaches  $\bar{\mu}/\beta$ , which occurs if the observer is close to the spanwise direction  $x_2$  (small values of  $x_1/S_0$  and  $x_3/S_0$ ). In this case the dipole-like directivity factor  $x_3/S_0$  makes the PSD go to zero according to Eq. (1), and the back-scattering correction becomes apparently irrelevant. Nevertheless, the applications of Section 5.3 will show that this correction can yield differences up to 2 dB even at relatively high frequencies. For this reason, it was kept in all calculations for the sake of completeness. The three-dimensionality, corresponding to oblique incident pressure gusts, is assessed more specifically in this section, as a necessary topic when addressing a finite aspect ratio.

Introducing the dimensionless acoustic wavenumber  $\bar{k} = kc/2$ , and assuming a Corcos' model for the spanwise coherence for the sake of simplicity [8], Eq. (1) specified in the mid-span plane can be written as

$$S_{pp}(\vec{x}, \omega) = \left( \frac{x_3 L}{2\pi S_0^2} \right)^2 \frac{2\bar{k}^3}{\pi b_c M_c} \Phi_{pp}(\omega) \int_0^\infty \text{sinc}^2 \left\{ \frac{L}{c} \bar{K}_2 \right\} \frac{|\mathcal{J}(\bar{k}/M_c, \bar{K}_2)|^2}{\bar{K}_2^2 + (\bar{k}/(b_c M_c))^2} d\bar{K}_2$$

where the symmetry is used to reduce the integral to the positive range of wavenumbers  $\bar{K}_2$ .  $b_c$  is the non-dimensional parameter of Corcos' spanwise correlation length (given for instance in Table 1 in Ref. [18]) and  $M_c = U_c/c_0$  the convection Mach number. In the same way, Eq. (2) reads

$$S_{pp}^\infty(\vec{x}, \omega) = \left( \frac{x_3}{2\pi S_0^2} \right)^2 L c \bar{k} b_c M_c \Phi_{pp}(\omega) |\mathcal{J}(\bar{k}/M_c, 0)|^2$$

the superscript  $\infty$  standing for an arbitrary large aspect ratio. Finally, the effect of the aspect ratio is assessed by checking the following quantity against 1:

$$\frac{S_{pp}}{S_{pp}^\infty} = \frac{2L}{\pi c} \left( \frac{\bar{k}}{b_c M_c} \right)^2 \int_0^\infty \frac{\text{sinc}^2(\bar{K}_2 L/c)}{\bar{K}_2^2 + (\bar{k}/(b_c M_c))^2} \frac{|\mathcal{J}(\bar{k}/M_c, \bar{K}_2)|^2}{|\mathcal{J}(\bar{k}/M_c, 0)|^2} d\bar{K}_2 \quad (9)$$

Sample results are given in Fig. 2, for Mach numbers of 0.05 and 0.5, and airfoil parameters corresponding to the ECL experiments described in the next sections. The computations have been performed including the leading-edge correction. The aspect ratio is varied from 0.5 to 10 and the values of  $AR = S_{pp}/S_{pp}^\infty$  plotted in decibels. It is found that an aspect ratio of 3 is enough to ensure good results in the mid-span plane using the asymptotic formula given by Eq. (2). This value is precisely the one retained in the experiments of next section. However, a significant error of a couple of decibels is expected if the aspect ratio is about one or smaller, and the full expression given by Eq. (1) is required in that case. This remains especially crucial at low speeds, even at relatively high frequencies. Small values of the aspect ratio must be considered in practice for fan noise prediction when a blade is split into segments, due to the different flow speeds and wall-pressure statistics

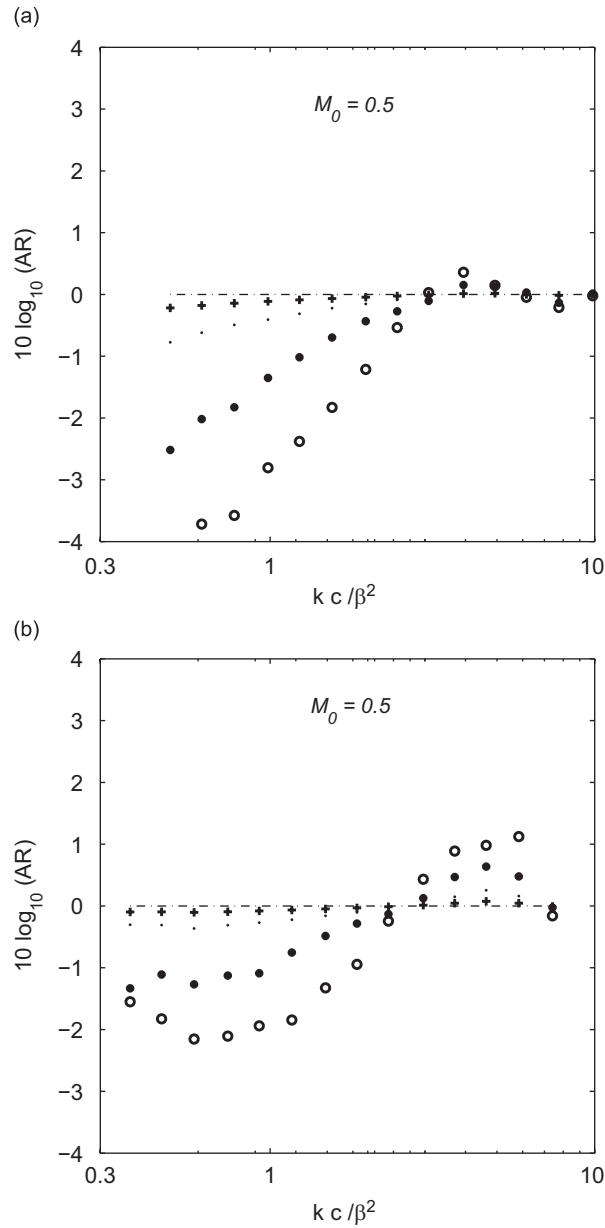


Fig. 2. Effect of the aspect ratio on the far-field radiation of a rectangular airfoil in the mid-span plane.  $c = 10$  cm,  $L/c = 0.5(\circ)$ ,  $1(*)$ ,  $3(\cdot)$ ,  $10(+)$ .

encountered at different blade radii. In view of the results, the general expression is more obviously dedicated to rotating blades, whereas the simplified form is relevant to the comparison with wind-tunnel measurements on isolated airfoils. For this reason, Eq. (2) is the only one used later on in the present study.

### 3. Experimental background

This section shortly addresses some key features of recent ECL experiments dedicated to the validation of the above extended Amiet’s model. The comparison between the model predictions and the experimental data is shown in the following Sections 4 and 5.

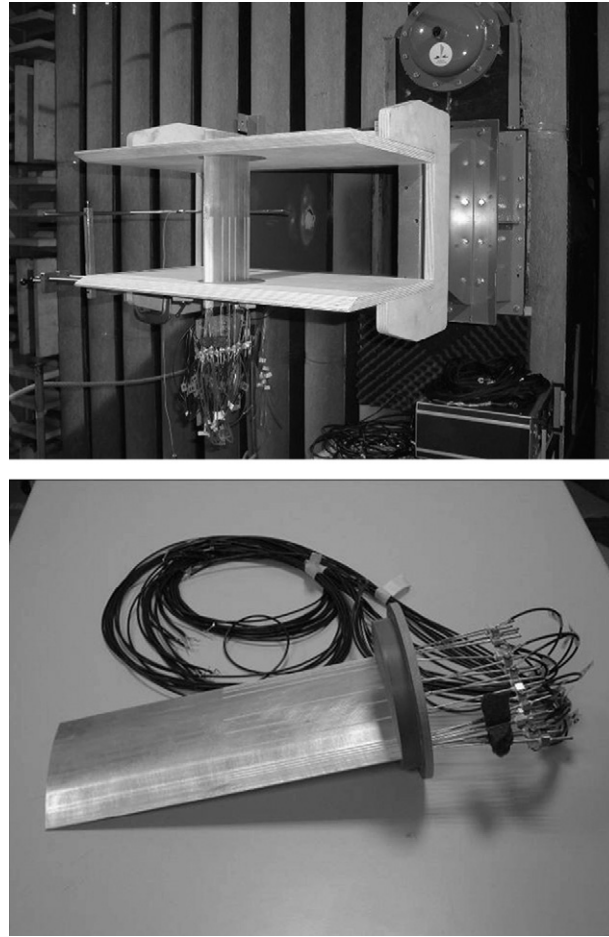


Fig. 3. Top: experimental set-up (ECL). Bottom: instrumented CD airfoil mock-up.

### 3.1. Experimental set-up

As mentioned in Ref. [21], pure airfoil self noise is better measured by placing the airfoil in a large quiet environment such as an open free-jet anechoic wind tunnel. The ECL-LMFA (Laboratoire de Mécanique des Fluides et Acoustique de l'Ecole Centrale de Lyon) has two such facilities: one smaller wind tunnel with dimensions ( $6\text{ m} \times 5\text{ m} \times 4\text{ m}$ ), flow capabilities ranging from 0 to 50 m/s and jet widths ranging from 0.13 to 0.3 m and a larger wind tunnel with dimensions ( $10\text{ m} \times 8\text{ m} \times 8\text{ m}$ ), flow capabilities ranging from 0 to 160 m/s and jet widths ranging from 0.13 to 0.6 m. As shown in Fig. 3 (left), the airfoil is held between horizontal side-plates fixed to the nozzle of the wind tunnel [15,22,23]. Two rotating discs inside the plates allow adjusting the angle of attack with respect to the flow. In the ECL experiments, typical mock-up chords are about 0.1 m (3.9 in) and span lengths about 0.3 m (11.9 in), fitting the nozzle height. The flow conditions are set by varying the angle of attack of the investigated airfoil and the flow rate through the nozzle of the wind tunnel. Placed in the potential core of a jet of limited width, the lifting airfoil induces a flow deflection. The measured wall-pressure distribution is then different from what would be found in free air, as pointed out by Moreau et al. [21]. The far-field noise is measured simultaneously using a single microphone in the mid-span plane, so that the transfer function between the wall-pressure fluctuations and the acoustic pressure can be deduced. The actual lift is determinant for the wall-pressure statistics but the transfer function only involves the airfoil geometry and is independent of the flow conditions. The same procedure can be repeated with the same installation on different airfoils or bodies at various flow conditions.

The present data base includes measurements performed on a reference symmetrical NACA-0012 airfoil (0.1 m chord length), a thin cambered Control-Diffusion airfoil (0.136 m chord length, 4% relative thickness and a  $12^\circ$  camber angle) designed by Valeo and a flat plate (0.1 m chord length and 3% relative thickness) [24]. The aim is to check the validity of the analytical prediction scheme on airfoils of different cambers and/or thicknesses, and different angles of attack. The typical flow conditions considered here are free-stream velocities ranging from 10 to 40 m/s, which corresponds to Reynolds numbers based on the airfoil chord length  $Re_c$  of about  $1.5 \times 10^5$  to  $6 \times 10^5$ , and Mach numbers of 0.1 representative of fan noise applications. More precisely, the NACA-0012 airfoil will be used in Section 4.3 to validate the predicted directivity patterns for a flow regime involving Tollmien–Schlichting (TS) waves. The other two will be used to investigate the broadband trailing-edge noise due to different turbulent flow regimes.

The case of a flat plate inclined in a flow is of great importance, both as a configuration encountered in many industrial fans and as an application with zero camber. It features two different mechanisms. On the suction side, the flow generally separates at the leading edge and reattaches farther downstream, forming a turbulent boundary layer. The turbulence is generated in the shear layer of the separation bubble and radiates noise when convected past the trailing edge. This is responsible for a true broadband signature. Furthermore, at moderate angles of attack, the attached flow around the trailing-edge rolls up in the wake, leading to a von Kármán vortex street and the resulting vortex-shedding sound. This part of the signature is narrow-band in nature, around the Strouhal frequency  $f_0 = 0.2U_0/e$ ,  $e$  being the plate thickness. As a result, the flat plate is suitable for the study of both trailing-edge noise and vortex-shedding noise, understood as different mechanisms. Pure trailing-edge noise is generated as upstream boundary-layer disturbances are convected past the trailing edge, whereas vortex-shedding noise involves the potential pressure field associated with vortices forming farther downstream, in the near wake. The latter mechanism cannot be handled by means of the present analytical model and will be ignored in the following. Yet the measured data helped defining a new ad-hoc model for vortex-shedding noise [25].

### 3.2. Instrumentation and measurements

The investigated airfoil is instrumented with flush mounted remote microphone probes (RMPs) [26] at mid-span in the streamwise direction on both suction and pressure sides of the airfoil, as shown in Fig. 3 (right). Additional probes are distributed in the spanwise direction close to the trailing edge. The RMPs allow the measurements of both the mean wall static pressure, used to infer the mean loads, and the fluctuating pressure statistics. Such probes are made of a spanwise flush mounted capillary tube with a pin hole at the measuring point. The capillary is then progressively enlarged outside the mock-up till a small Electret microphone can be flush mounted. The Electret microphones have the required sensitivity (up to 10 kHz) for the present investigation. A long closed PVC tube is connected to the outer end of the capillary in order to attenuate longitudinal waves and prevent spurious flow inside the tube. Details of the technology and the calibration of the sensors can be found in Ref. [27]. The calibration is first made after building the sensor by comparing its response to the equivalent response of a reference B&K 1.27 cm (1/2 in) Type-4181 microphone. Further in situ calibration has been achieved with a B&K Type-4228 pistonphone at 1 kHz, placed on the pinholes of the sensors. During the experiment, the signal measured by each Electret microphone is transferred through an amplification stage to a 16 channels HP3565 Paragon FFT analyser. Standard B&K 1.27 cm (1/2 in) Type-4181 microphones placed on a moving arm in the far field simultaneously collect the acoustic spectra. Finally, tuft visualisations are used to qualitatively estimate the flow separation zones and a single hot wire is raked to measure the wake velocity profile close to the trailing edge.

### 3.3. Angle-frequency radiation maps

Typical far-field data are shown in this section to point out some key features of the sound field, as measured in the wind tunnel. They are presented as radiation maps for the flat plate and the CD airfoil, the acoustic level being plotted as a function of the radiation angle and the frequency. The background noise obtained when the airfoil or the plate is removed has been subtracted according to the procedure described in

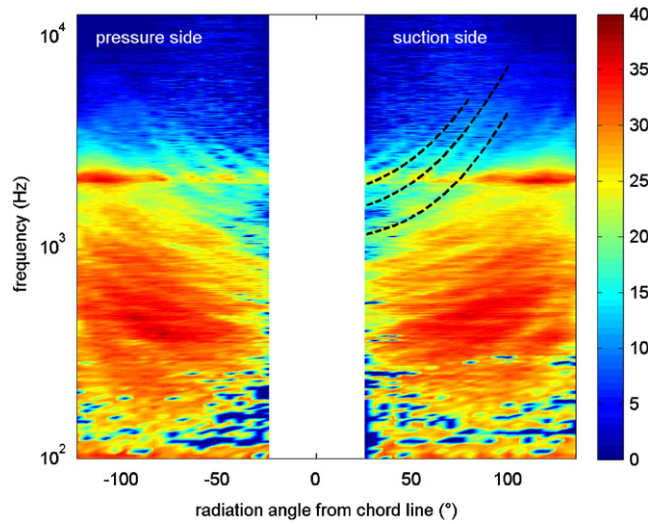


Fig. 4. Angle-frequency radiation map for the flat plate at  $5^\circ$  angle of attack, showing both trailing-edge noise and vortex-shedding noise.  $U_0 = 30$  m/s, decibel scale on the right side.

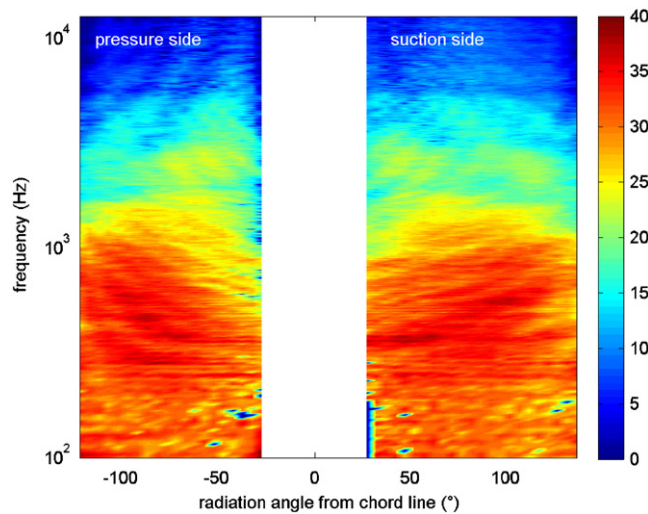


Fig. 5. Angle-frequency radiation map for the CD airfoil at  $15^\circ$  angle of attack, showing pure trailing-edge noise.  $U_0 = 30$  m/s, decibel scale on the right side.

Ref. [18]. The actual level is given as

$$|S_{pp}|_{dB} = SPL_2 + 10 \log_{10}(1 - 10^{(SPL_1 - SPL_2)/10})$$

where  $SPL_1$  and  $SPL_2$  denote the measured levels in dB corresponding to the background noise and the noise with the mock-up installed. These maps provide an easy overview of a large amount of data and as such, they are a convenient way to illustrate the main trends to be reproduced by the model. Furthermore, they help to identify possible wind-tunnel set-up effects. Quantitative comparisons between the measurements and the model will be achieved in the next sections, by means of single-frequency directivity diagrams and single-angle noise spectra. Such plots are simply horizontal and vertical cuts in the radiation maps, respectively.

The radiation maps are plotted in Figs. 4 and 5, for a flow speed of 30 m/s. The available range of radiation angles is from  $25^\circ$  to  $115^\circ$ , typically, with respect to the downstream chordwise direction. Smaller angles

correspond to observation points inside the wind-tunnel jet flow, for which the microphone measures the pseudo-sound associated with the jet turbulence. This information is removed from the data set. Higher angles cannot be covered due to the absorbing walls of the anechoic room. Fig. 4 clearly exhibits the separated contributions corresponding to the pure broadband trailing-edge noise and the vortex-shedding noise in the case of the plate [25]. The former covers the low and medium frequency range up to more than 1 kHz, whereas the latter is a narrow-band feature at the significantly higher Strouhal frequency, around 2 kHz. The inclined and curved secondary patterns indicated by dashed lines in Fig. 4 are interference fringes attributed to an acoustical installation effect: since the airfoil must be embedded in the potential core of the wind-tunnel jet, the radiated sound field of interest is contaminated by some scattering at the nozzle lips and on the side-plates. This is crucial for self-noise at higher frequencies, for which sound focuses upstream, as well as at lower frequencies because of the proximity of the nozzle in terms of acoustic wavelengths. The interference fringes are also responsible for the spots at their intersections with the vortex-shedding narrow-band signature. They will contribute to some of the discrepancies seen in the comparisons of predicted and measured directivity diagrams and spectra in Sections 4.3 and 5.2. Another very important feature clearly seen on the map is that the amplitude of the sound field is symmetric with respect to the chord line, despite the strong imbalance of the flow field between the suction side and the pressure side at this angle of attack. This is expected from the analytical model and the dipole-like behaviour of the equivalent sources.

The radiation map for the CD airfoil at significant aerodynamic loading is shown in Fig. 5. It exhibits the same typical broadband signature as for the plate; no vortex shedding occurs here, because the effective thickness of the rounded trailing edge, less than 1.5 mm, is smaller than the boundary-layer thickness. The asymmetry of the radiated field is hardly seen, because the camber effect is expected to be small in decibels in view of the theoretical results plotted in Section 4.2, Fig. 7. This provides a first validation of the flat-plate assumption in the model: a thin, moderately cambered airfoil radiates trailing-edge noise almost symmetrically. Higher camber angles would certainly make the measurements depart from this trend.

#### 4. Single-frequency directivity

As mentioned above, a first quantitative comparison of the analytical model with other data is provided by looking at the far-field pressure directivity in the mid-span plane for various fixed frequencies. This can be achieved by considering the radiation integral  $\mathcal{I}$  times  $kc \sin \theta$  or equivalently the aforementioned ratio  $\mathcal{A}$ . In the subsequent subsections, the current directivity predictions are compared at several frequencies with previous analytical models, with numerical simulations, and with airfoil measurements.

##### 4.1. Comparison with analytical models

The extended Amiet's solution is first compared to the recent analytical results of Howe [14], for the far-field acoustic pressure associated with an airfoil of arbitrary chord length. In this work, Howe derived a composite Green's function valid for all values of the reduced wavenumber  $kc$ , by combining an approximate Green's function valid for small  $kc$  and another one valid for large  $kc$ . The former extrapolates Green's function for an airfoil of acoustically compact chord to small finite  $kc$ . The latter takes into account the multiple wave scattering at the airfoil leading and trailing edges. The approximate Green's functions of the scattered fields [10,28] are obtained by the Wiener–Hopf technique iteratively. The sum of all these contributions yields a series that converges absolutely for  $kc > \frac{1}{2}\pi$ . Fig. 6 shows that the present analytical model agrees very well with Howe's calculations for the four considered frequencies. At low frequencies ( $kc \leq 2\pi$ ), the sound directivity has two symmetric lobes typical of a compact dipole. With increasing high frequencies ( $kc > 2\pi$ ), the sound directivity exhibits more and more additional lobes. Such a good agreement is to be expected from Fig. 4 in Ref. [14] where the double scatter (equivalent to the present leading-edge back-scattering) collapses with the multiple scatter for all  $kc > 1$  (for  $\psi = 90^\circ$ ). This is also a confirmation of the formal correspondence between the current model based on the iterative Schwarzschild's technique [29,30] and the Wiener–Hopf procedure used by Howe.

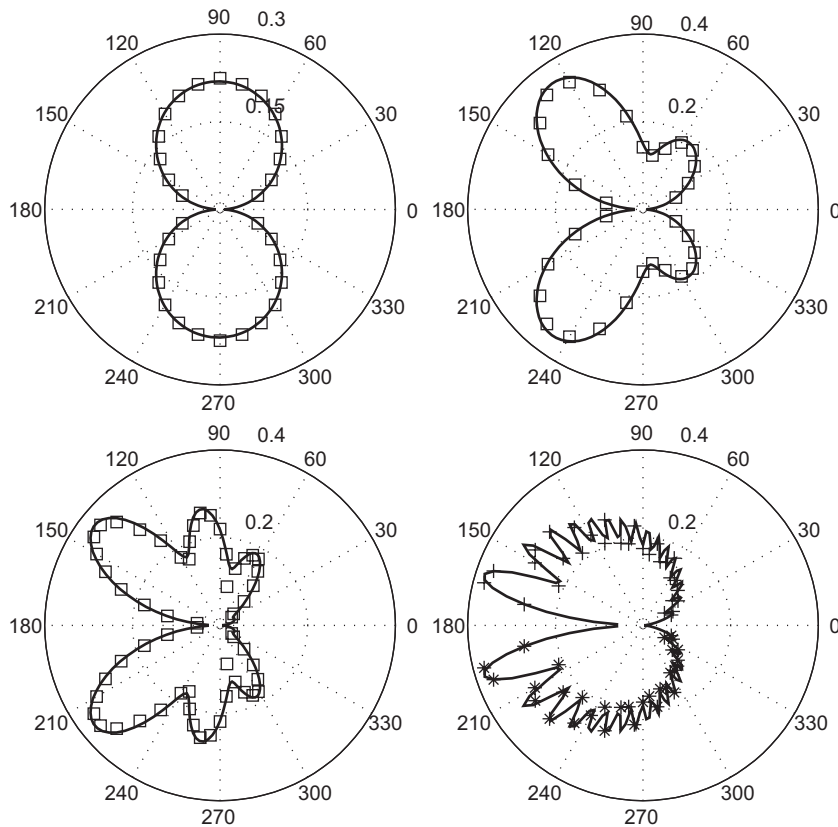


Fig. 6. Directivity patterns at several frequencies. From left to right and top to bottom:  $kc = 1, 5, 10, 50$ .  $M_0 = 0.05$ . — Present full solution, symbols: Howe's analytical model.

#### 4.2. Comparison with simulations

The single-frequency analytical transfer function for the flat plate with a finite chord length can be compared to numerical simulations to assess the importance of some ignored parameters, such as camber and thickness. In Refs. [31,32], Oberai et al. numerically solved a variational formulation of Lighthill's acoustic analogy by a finite element method, to assess the trailing-edge noise of a two-dimensional airfoil. They recasted the analogy into a three-dimensional non-homogeneous Helmholtz equation for the acoustic pressure by applying a time Fourier transform. The right-hand-side source term can be constructed from an independent large eddy simulation (LES) in the vicinity of the trailing edge [32,33]. The Helmholtz equation is then solved in the acoustic near field, typically inside a cylinder enclosing the airfoil. Sommerfeld's condition at infinity is replaced by an equivalent non-reflecting boundary condition at the cylinder surface. The procedure involves a linear integro-differential operator or Dirichlet-to-Neumann map. On the airfoil surface, a sound-hard boundary condition is applied. This is equivalent to use a Green's function tailored to the airfoil geometry rather than the semi-infinite flat plate used in Refs. [11,33]. In this particular acoustic problem, a space Fourier transform in the spanwise direction yields a simplified two-dimensional problem outside the near-field boundary, taking advantage of the cylindrical topology. The far-field noise is finally obtained analytically by expanding the computed near-field acoustic pressure into a series involving Hankel functions of the first kind.

In Ref. [32], this methodology was applied to a slightly cambered Eppler 387 airfoil at a  $2^\circ$  angle of attack. The results were shown to be highly dependent on the source distribution. To avoid possible numerical errors related to the flow simulation, the far-field pressure directivity was also investigated using simple quadrupole sources placed near the trailing edge of the airfoil. The computed directivities are compared with the present

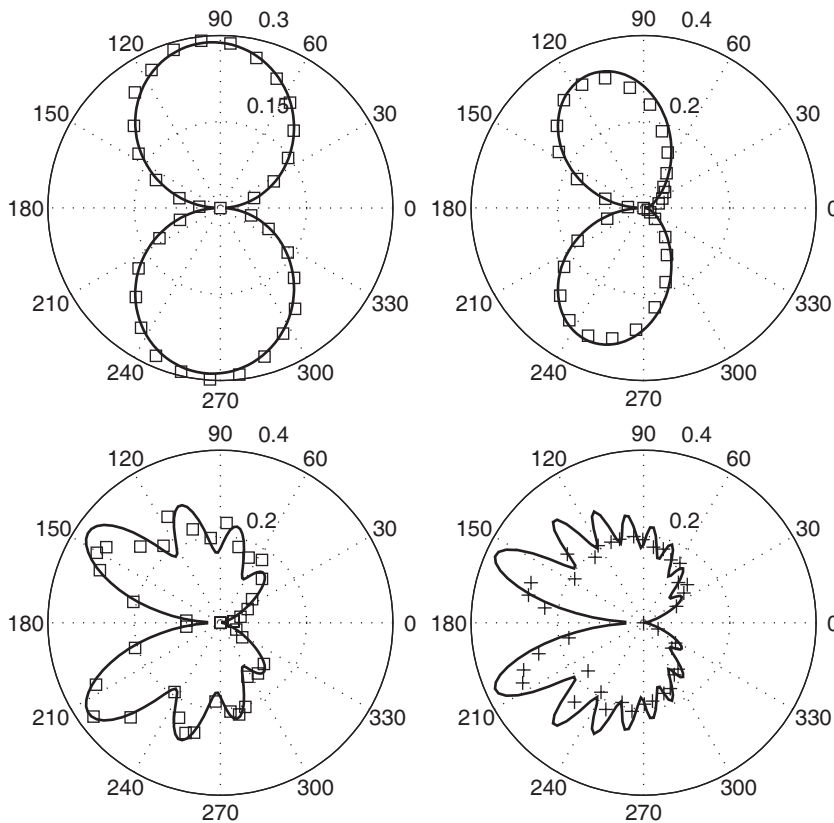


Fig. 7. Directivity patterns at several frequencies. From left to right and top to bottom:  $kc = \frac{\pi}{2}, \pi, 4\pi, 8\pi$ .  $M_0 = 0.05$ . — Present full solution, symbols: Oberai et al. simulation.

analytical model in Fig. 7 for increasing frequencies. The same trend as in Fig. 6 is again found. At low frequencies, for  $kc$  below  $2\pi$ , the directivity is similar to that of a compact dipole. For higher frequencies, the airfoil is no longer compact and the directivity has more and more lobes. The flat-plate assumption made in the analytical model does not allow reproducing the slight differences between sounds radiated from the pressure and suction sides but the errors remain very small in terms of decibels. This suggests that the analytical solution can be used with benefit for any airfoil shape with moderate thickness and camber.

#### 4.3. Comparison with present experiments

The best experimental way to check the model directivity irrespective of the flow conditions is to generate trailing-edge noise sources with tonal excitation. This has been done here with a NACA 0012 airfoil at zero angle of attack in the anechoic open-jet wind tunnel of the ECL. In that configuration, the boundary layers are laminar and unstable in the aft part of the airfoil, leading to the onset of TS waves [34,35]. Direct trailing-edge noise is radiated as the TS waves are convected past the trailing edge. Furthermore, due to acoustic back-reaction [34], self-sustained oscillations occur at discrete frequencies that are amplified, leading to strong tones superimposed on the direct noise. An isolated tone is associated with wall-pressure fluctuations that are almost perfectly spanwise-correlated because triggered by the acoustic waves generated at the trailing edge [18]. For that reason, the isolated TS radiation is a nearly two-dimensional process with respect to an observer in the distant mid-span plane and, as such, is the best experimental illustration of the basic analytical solution given by Eq. (17) or (18) with Eq. (20) of part I [8]. Therefore measured and computed directivity patterns should agree at best.

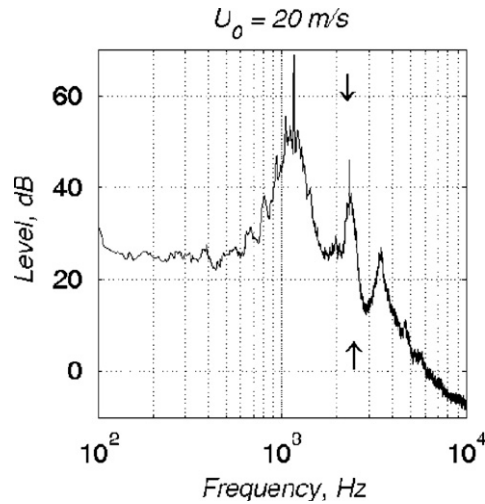


Fig. 8. Far-field noise spectrum for TS wave radiation of a NACA0012 airfoil at  $U_0 = 20$  m/s and  $0^\circ$  angle of attack.

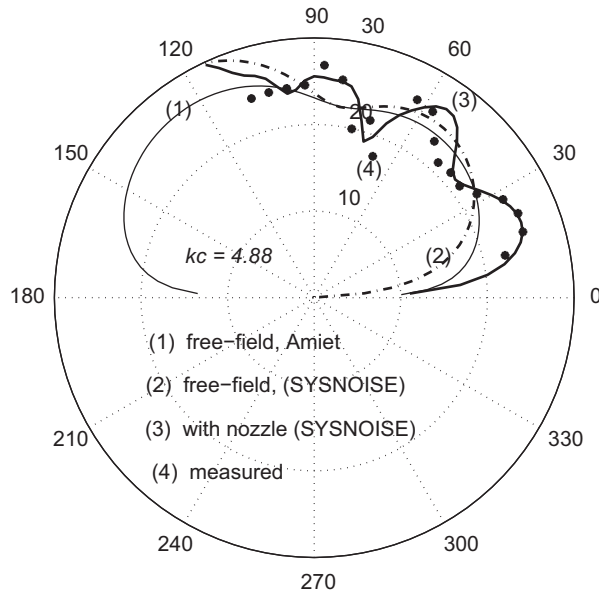


Fig. 9. Measured and computed directivities for TS wave radiation. Levels in relative decibels. NACA0012 airfoil at  $U_0 = 20$  m/s and  $0^\circ$  angle of attack.

A typical noise spectrum associated with the onset of TS waves is shown in Fig. 8. A dominant high-level tone around 1200 Hz and a narrow-band hump corresponding to the direct acoustic radiation are clearly observed. The flow speed of 20 m/s is a relatively high flow regime with respect to the onset of TS waves, in the sense that even higher speeds would progressively trigger transition to turbulence in the boundary layers and saturate the TS waves. It is chosen here to get higher tone frequencies. A secondary pattern (and even a less noticeable third one) appears at twice the primary frequency range, attributed to nonlinearity in the instability phenomenon. The harmonic tone around 2500 Hz (shown by the arrows in Fig. 8) has been selected here for the directivity validation, to take advantage of the multiple radiation lobes expected for a non-compact source. The corresponding reduced frequency  $kc$  is indeed about 5. The directivity measurements over the angular range covered in the experiment at  $kc \approx 5$  exhibit a three-lobed pattern in the first quadrant, as shown in relative decibels in Fig. 9 (symbols (4)). The analytical free-field solution (thin solid line (1)), ignoring the

nozzle effect, is strongly different and shows only two lobes consistently with Fig. 6. The levels have been adjusted using an arbitrary constant since only the directivity is addressed here. This totally different behaviour has been attributed to sound diffraction at the nozzle lips, that are shaped with corners. The nozzle diffraction can be expected to be significant for any angle of radiation in view of the short distance between the nozzle and the mock-up in the experiment (Fig. 3). It has been evaluated numerically in a two-dimensional configuration in the mid-span plane using the commercial propagation code SYSNOISE. In the numerical simulation of the Helmholtz equation at 2500 Hz, the airfoil is meshed as a flat plate with a 3% relative thickness. A scattering correction is defined as the difference between the computed fields of the plate in free field and in the presence of the nozzle. An approximate correction is computed by placing two out-of-phase elementary sources on each side of the plate at the trailing edge. The latter mimic the sound generation occurring at the trailing edge because of the sudden change in the vorticity. This does not mean that the airfoil is considered as a compact source. In the analytical model, the equivalent acoustic sources are distributed along the chord length and are assumed to radiate in free field. They account for the scattering of trailing-edge sources by the non-compact airfoil surface since the model is compressible. In the SYSNOISE simulation, the scattering by the airfoil is explicitly computed in the same way as the scattering by the nozzle lips. Though some uncertainty results from this simple approach, a relatively good agreement is found by comparing the free field computed in the absence of the nozzle (dashed-dotted line (2)), and the exact analytical solution (thin solid line (1)). This justifies the choice of the two elementary sources. The corrected analytical results (thick solid line (3)), also plotted in Fig. 8, now agree well with the measurements.

The TS wave radiation cannot be used to validate Eq. (6) in a more quantitative way. Indeed, the radiation integral ( $kc\mathcal{I} \sin \theta$ ) does not involve precise flow conditions, except for the mean flow speed and a convection speed. It holds for any kind of incoming wall-pressure disturbances, deterministic or random. The full equation (6), however, assumes randomly distributed disturbances with a spanwise coherence length much smaller than the span. These assumptions do not apply to the TS tones used here for the directivity validation at a single frequency. Finally it is important to stress that the nozzle scattering can significantly distort the direct radiation field from the investigated sources in any similar experiment [36]. The scattering effect, often ignored, should always be evaluated and included when comparing noise predictions with experimental results.

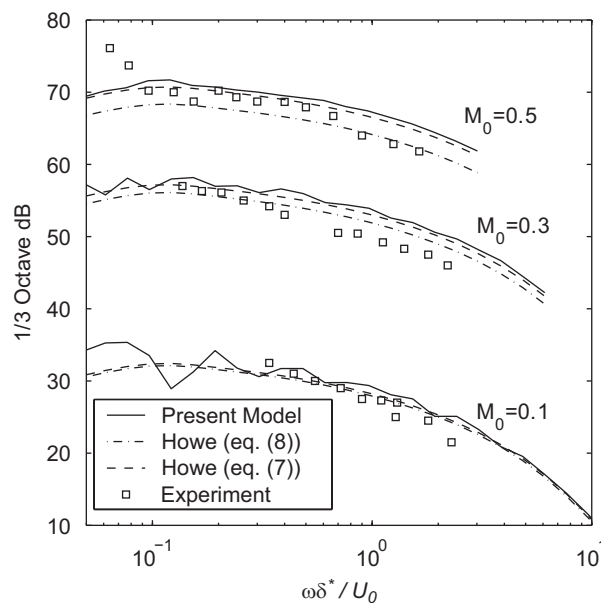


Fig. 10. Trailing-edge noise model predictions compared to the experimental results of [23]. Helicopter blade airfoil, microphone in the mid-span plane at  $70^\circ$  from the chord line.

## 5. Noise spectra

A complementary assessment of the present model is provided by looking at the spectral distribution of the far-field PSD,  $S_{pp}$ , at a given observer position  $(R, \psi, \theta)$  [18]. In the subsequent sections, the current far-field acoustic predictions are compared with previous and recent ECL measurements on various bodies, in the mid-span plane ( $\psi = 90^\circ$ ) in a direction almost perpendicular to the chord line ( $\theta \simeq 90^\circ$ ).

### 5.1. Previously reported experiments

The first set of experimental data used to assess the validity of the present prediction method are the far-field noise spectra measured around a helicopter rotor blade by Schlinker and Amiet [23]. Three different Mach numbers of 0.1, 0.3 and 0.5 were tested in the UTRC anechoic wind tunnel. The mock-up had a 0.41 m chord length and a 0.3 m span. The wall-pressure fluctuations,  $\Phi_{pp}$ , were not measured in that experiment. The separate data of Yu and Joshi collected on a NACA-0012 profile were used instead [37]. Similarly, the convection speed and the spanwise correlation length as measured by Willmarth and Roos on a flat plate were introduced in the calculations [5,38]. The acoustic measurements were made in the mid-span plane with a directional microphone, for an observer distance of 3 m and an angle  $\theta = 70^\circ$ . The results are shown in Fig. 10, where the far-field third-octave spectra are plotted as a function of the Strouhal number based on the displacement thickness at the trailing edge and the incoming velocity. The present model predictions (Eq. (6)) are also plotted in the figure and compared with Howe's asymptotic model (Eqs. (7) and (8)). The predictions of Ref. [23] ignoring the leading-edge back-scattering, not shown here, and the present ones agree very well, except for lower levels at lower frequencies (smaller  $kc$ ), where the correction of part I becomes significant. This in turn brings a slightly better agreement of the present model with the measurements. Yet at lower frequencies (Strouhal number below 0.1), the measured spectra clearly exhibit another noise source suggested by the strong change of slope observed at  $M_0 = 0.5$ . The predictions using the simplified version of Howe's asymptotic model, Eq. (8) (dotted lines) depart progressively from the present ones as the Mach number increases. If the Mach number correction  $(1 - M_c)^{-1}$  found in Eq. (7) is reintroduced in Eq. (8) (dashed lines), a much better agreement is found. This emphasises that Eq. (8) should be used below a Mach number of 0.3. It should be noted, however, that uncertainties and inaccuracies lie in the lack of direct measurements of the

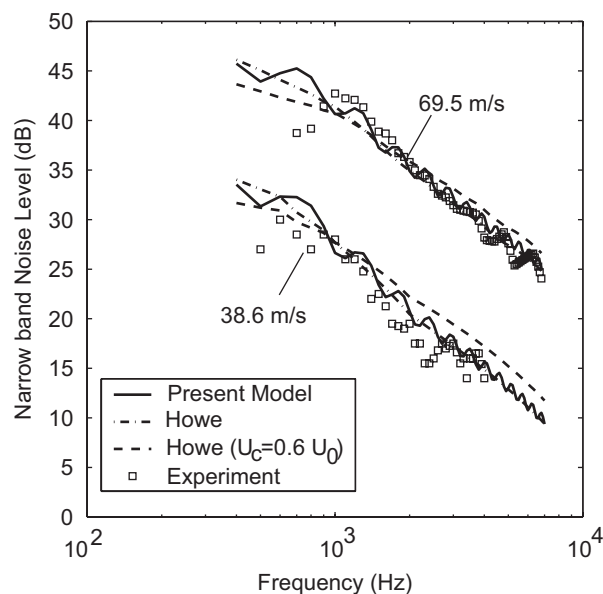


Fig. 11. Trailing-edge noise model predictions compared to the experimental results of [15]. NACA-0012 airfoil, microphone in the mid-span plane at  $90^\circ$  from the chord line.

wall-pressure statistics and of precise information on the speed of sound, tunnel velocity and boundary-layer thickness at the trailing edge. Resolution issues have also been pointed out by Brooks and Hodgson [15].

The second comparison involves the more complete experimental data base of Brooks and Hodgson obtained in the anechoic quiet-flow facility of NASA Langley Research Center [15]. The airfoil used in this test was a NACA-0012 airfoil with a chord length of 0.61 m and a span of 0.46 m. The flow conditions were varied from about 20 to 70 m/s with three different angles of attack of  $0^\circ$ ,  $5^\circ$  and  $10^\circ$ . Surface pressure spectra were measured at the same time as the far-field noise spectra. Special Kulite transducers were clustered in the trailing-edge portion of the mock-up for the surface data, whereas the far-field measurements involved eight B&K 1.27 cm (1/2 in) Type-4133 microphones. The flow field was also fully characterised around the airfoil using tufts, Preston and Pitot tubes and hot wire rakes. All the measured quantities of Ref. [15] have been included in the present simulation: spanwise correlation lengths and convection speeds close to the trailing edge deduced from the cross-spectral measurements between surface sensors, as well as their variation with frequency (Figs. 18–21 in Ref. [15]). The comparison between analytical predictions based on the present solution and on the asymptotic Howe's model, on the one hand, and the far-field noise measured on the NACA-0012 airfoil at  $0^\circ$  incidence, on the other hand, is shown in Fig. 11 for the two flow speeds 38.6 m/s ( $M_0 = 0.11$ ) and 69.5 m/s ( $M_0 = 0.2$ ). For this application, the finite-span correction calculated from the formulae of Section 2.2 has been included in the extended Amiet's model. A very good agreement is obtained. Furthermore, the predictions using Howe's low Mach number model agree very well with Brooks and Hodgson's calculations based on the full equation (4) (Fig. 40 in Ref. [15]). The oscillations observed with the present model are attributed to the non-compactness at the high reduced acoustic wavenumbers,  $kc \geq 10$ , met in this experiment. They result from the Fresnel integrals in the formulation. The weaker oscillations in the measurements might be due to additional interference with the nozzle scattering or the downstream collector reflection. The COP method used in Brooks and Hodgson's experiment may attenuate these spurious effects by averaging over several microphones around the airfoil, but the averaging process also smoothes out the far-field spectra. Moreover, the multiple scattering of acoustic waves at the trailing and leading edges certainly is made less regular by the curvature of the airfoil surface and the propagation through the boundary layers, with respect to an ideal flat plate with uniform flow. Finally, the predicted noise levels are found to be very sensitive to input values. For instance, the effect of the convection speed is clearly seen in Fig. 11 by taking an average value  $\bar{U}_c = 0.6U_0$  over the whole frequency range (as shown in Fig. 40 in Ref. [15]), instead of a variable speed. On the one hand, the simplification leads to higher noise levels at high frequencies where the actual convection speed is lower. On the other hand, it triggers lower noise levels at lower frequencies where the actual convection speed is higher. Similarly, using the data of Yu and Joshi [37] or the flat plate measurements of Willmarth and Roos [38] as suggested above by Schlinker and Amiet would also degrade the results significantly. Therefore the relevant wall-pressure spectra, convection speed and spanwise correlation length should always be preferred to yield the proper spectral shape and level.

## 5.2. New experimental data base

Recent self-noise experiments have been run in the ECL open-jet anechoic wind-tunnel facilities involving two mock-ups with different cross-section shapes, namely a flat plate and a cambered CD (Controlled Diffusion) airfoil, in various flow conditions (tunnel speeds and angles of attack) and for two jet widths. The results significantly expand the aforementioned existing experimental data base on trailing-edge noise and include the measurements of all the parameters necessary to test the analytical model of part I. The flat plate has been tested for geometrical angles of attacks with respect to the incoming flow direction ranging from  $\alpha_g = 5^\circ$  to  $10^\circ$ , in a 13 cm width nozzle flow, at the two speeds of 20 and 40 m/s. The CD airfoil has been tested for geometrical angles of attacks between  $\alpha_g = -5^\circ$  and  $15^\circ$ , in both a 13 cm width nozzle and a larger 50 cm width nozzle, at the two speeds of 16 and 30 m/s.

As stated by the acoustic models, the far-field sound spectrum,  $S_{pp}$ , is related to the local trailing-edge wall-pressure spectrum assuming that the wall-pressure field is statistically homogeneous. This has been first verified for both the airfoil and the plate by accurately measuring the quantities  $\Phi_{pp}$ ,  $\ell_y$  and  $U_c$  using the RMPs (Section 3). Wall-pressure measurements on the flat plate were allowed quite close to the trailing-edge (between 3 and 6 mm upstream) thanks to the plate thickness and the small diameter of the capillary tubes

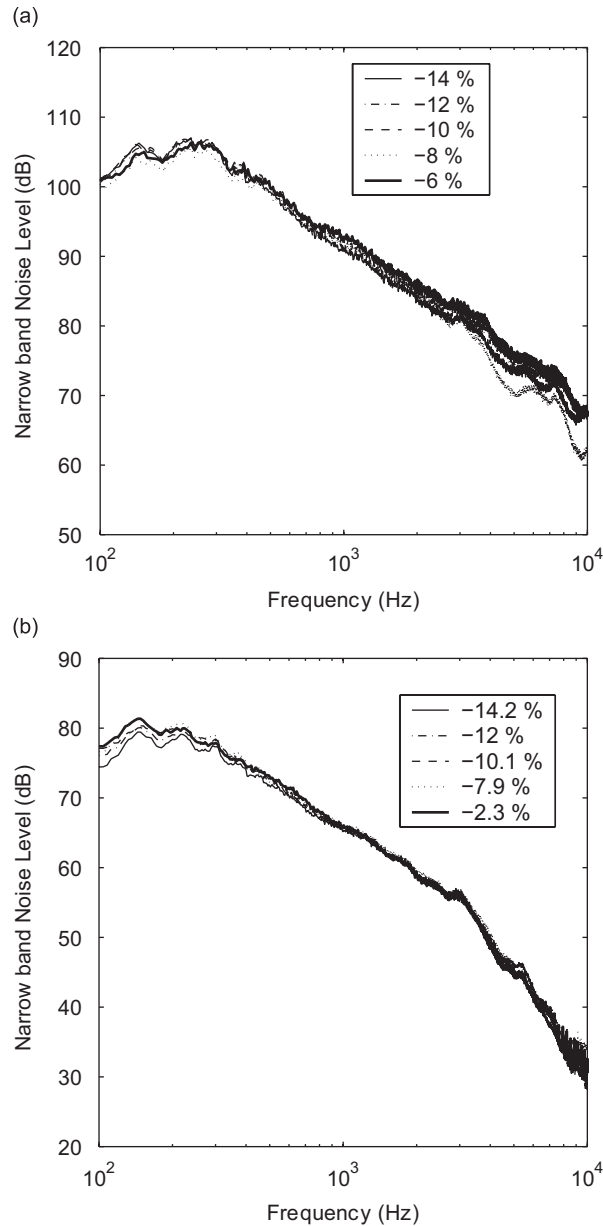


Fig. 12. Streamwise statistical homogeneity of the wall-pressure spectra for sensors close to the trailing edge. Distances from the edge in relative chord length: (a) flat plate—40 m/s, 10° angle of attack, (b) CD airfoil—16 m/s, 15° angle of attack.

used to manufacture the RMPs. This procedure is expected to ensure the best possible results, as far as the distance to the edge remains large enough with respect to the aerodynamic wavelengths of the boundary-layer disturbances to avoid contamination of the measurements by the edge scattering, according to the arguments of Brooks and Hodgson [15]. Figs. 12(a) and (b) show the corresponding wall-pressure PSD on the last five streamwise sensors closer to the trailing edge for the flat plate (left) and the CD airfoil (right). Both plots show a satisfactory homogeneity and the PSD measured at the last streamwise location has been chosen as the noise source input data in the simulations below. The spanwise homogeneity has been checked successfully as well. Both Eqs. (2) and (7) also rely on the assumption that the spanwise correlation length close to the trailing edge is much smaller than the spanwise extent  $L$  of the mock-up. The set of spanwise unevenly spaced RMPs, including the last streamwise sensor, has been used to assess this point. Figs. 13(a) and (b) show that at all

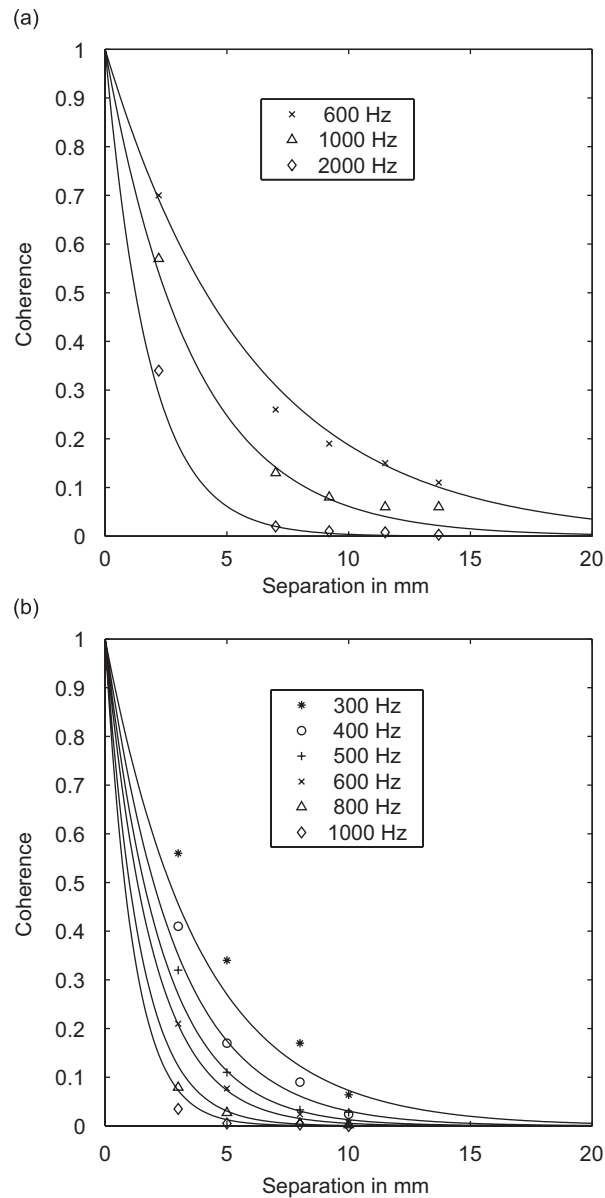


Fig. 13. Coherence plots between spanwise sensors close to the trailing edge. Symbols stand for measured values and continuous lines for a fitted Corcos' model: (a) flat plate—40 m/s, 5° angle of attack, (b) CD airfoil—16 m/s, 15° angle of attack.

frequencies the spanwise coherence for the flat plate (left) and the CD airfoil (right) decays exponentially with both frequency and sensor separation, according to a modified Corcos' model fitted on the data. The coherence is only significant for separations of about 10–15 mm, much smaller than  $L \simeq 300$  mm. Both model assumptions are therefore fulfilled. This was also clearly checked in the detailed, careful experiment of Brooks and Hodgson: Figs. 10 and 18 in Ref. [15].

The main comparisons of the predictions with the far-field measurements performed with the flat plate are first reported in Fig. 14 for a microphone in the mid-span plane, at a distance of 2 m and an angle of 90° with respect to the chord line. A good overall agreement is found, both with the present model and Howe's asymptotic model. Accounting for the leading-edge back-scattering in Amiet's theory has a significant effect at low frequencies below 400 Hz with an additional contribution of 2–3 dB and a smaller contribution at mid

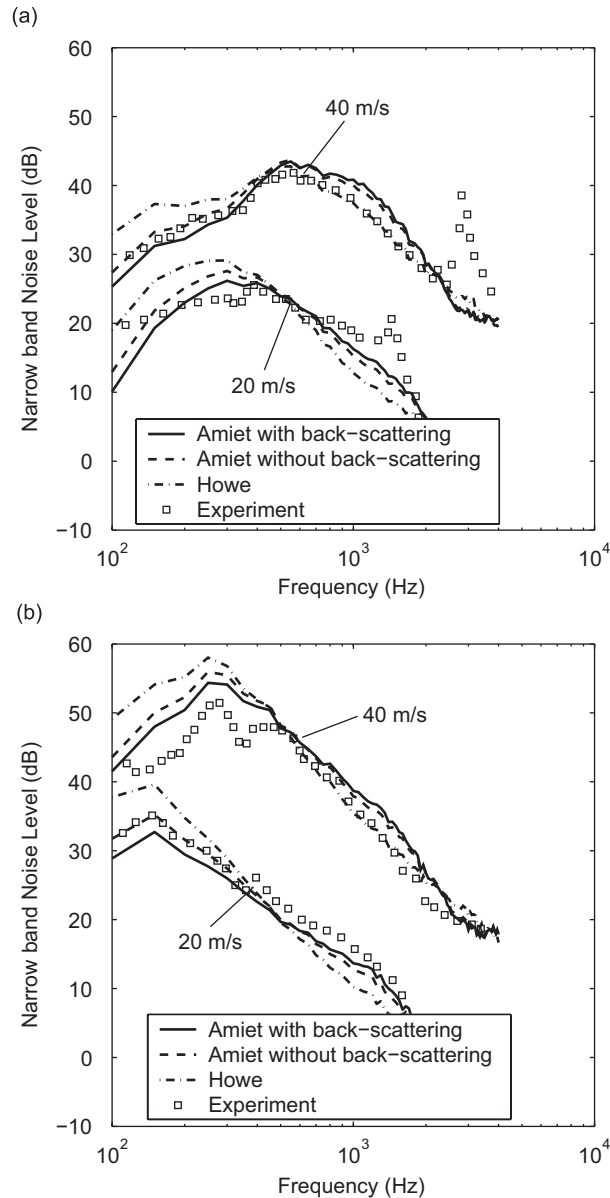


Fig. 14. Trailing-edge noise model predictions compared to the experimental results of Ref. [18]. Flat plate, microphone in the mid-span plane at 90° from the chord line: (a) 5° angle of attack, (b) 10° angle of attack.

frequencies between 800 and 2000 Hz where it yields a maximum level reduction of 1.5 dB. In Fig. 14, frequencies below 500 Hz correspond to values of  $kc$  smaller than 1, thus a compact chord length. In this range, though no directivity results are given here, the extended Amiet's model predicts a pure dipole-like two-lobe directivity pattern similar to the one of Fig. 6(a). In contrast the asymptotic model exhibits the cardioid pattern due to the term  $\sin^2\theta/2$ , irrespective of what the frequency could be, and is clearly irrelevant. At higher values of  $kc$ , both models tend to behave the same way, except for the multiple-lobe structure due to the finite chord length, as shown by the asymptotic trend of Amiet's solution discussed in Appendix A. Here both calculations provide the same order of magnitude at 90° to the chord line but would significantly differ at other angles, especially in the upstream half-space. Since the half-plane assumption cannot hold for the

compact chord case, it is not surprising that Howe's asymptotic model departs from both Amiet's model and the measurements at lower frequencies in Fig. 14, even at  $90^\circ$ .

At the angle of attack  $\alpha_g = 5^\circ$ , the flow separates at the plate leading edge and reattaches farther downstream, giving rise to a turbulent boundary-layer thin enough to allow for a von Kármán vortex shedding [40]. The corresponding peaks at 1400 and 2800 Hz in Fig. 14(a) cannot be reproduced by the present model since they involve vortical eddies formed in the wake instead of boundary-layer turbulence. The von Kármán vortex shedding does not occur anymore at the angle of attack  $\alpha_g = 10^\circ$  due to a much thicker boundary-layer thickness at the trailing edge. The fact that, despite the inappropriate assumptions, Howe's asymptotic model seems to fit the experimental values more closely than Amiet's model at some frequencies in Fig. 14 may be attributed to the scattering effect of the nozzle lips, already mentioned in Section 4 and not accounted for here in the predictions. The overall agreement is in favour of both approaches relating the far-field sound to the

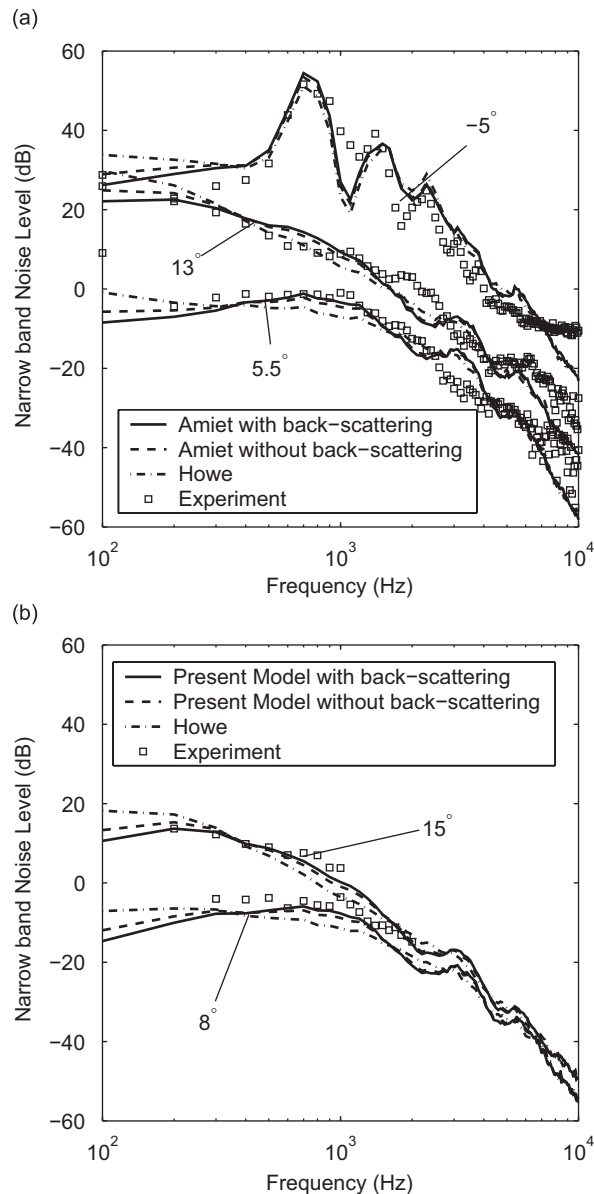


Fig. 15. Analytical trailing-edge noise model against experimental results of Ref. [18]; Valeo CD airfoil in the mid-span plane at  $90^\circ$ .

wall-pressure statistics. The present back-scattering correction slightly improves the comparison with the measurements.

The results for the CD airfoil embedded in two different ECL anechoic wind tunnels with a narrow nozzle (13 cm jet width) and a large nozzle (50 cm jet width) are considered next. Three different flow regimes already described in Ref. [18] are found on this airfoil when placed in the narrow nozzle: the attached turbulent boundary layer initiated by a large leading-edge separation at large positive angles of attack; the attached turbulent boundary layer triggered by a short laminar bubble, with some vortex shedding at the trailing edge for small or moderate angles of attack; and the laminar boundary layer with TS waves for small negative angles of attack. The denomination of short and long laminar separation bubbles follows the classification of Gaster [41]. In the preliminary study of Ref. [42], three different velocities, 30 m/s, 16 m/s and 10 m/s were considered to illustrate the aforementioned flow regimes. A good agreement was found between the measurements and the extended Amiet's model. The results presently analysed are focussed on the free-stream velocity of 16 m/s and the geometrical angle of attack  $\alpha_g$  is the only varied parameter. The value  $-5^\circ$  corresponds to the TS regime, the value  $5.5^\circ$  to the vortex-shedding regime and the value  $13^\circ$  to the turbulent regime. Again, the measured wall-pressure spectra, convection speeds and spanwise correlation lengths are used in the simulations. In particular, consistent models for the coherence, well different from Corcos' model

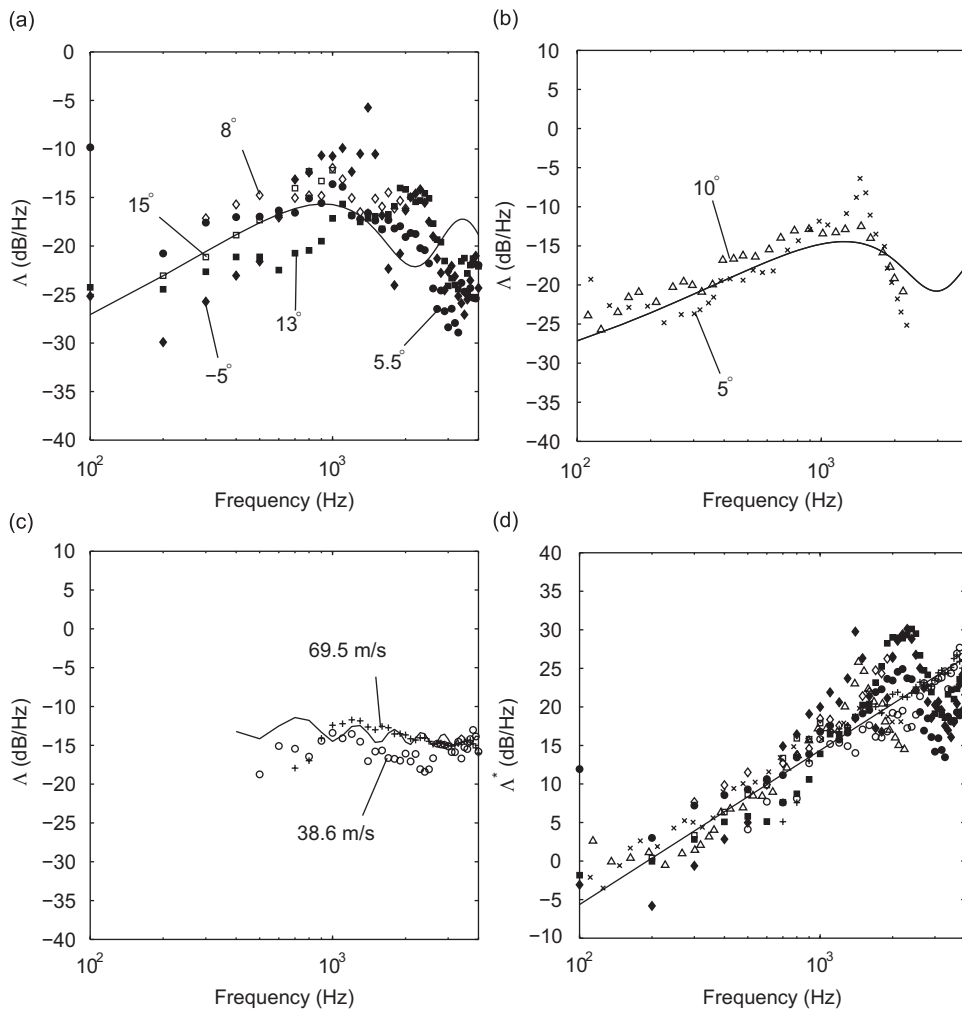


Fig. 16. Dimensionless invariants for trailing-edge noise at  $90^\circ$  with respect to the chord length: (a) CD airfoil—16 m/s, 13.6 cm-chord, (b) flat plate—20 m/s, 10 cm-chord, (c) NACA-0012, 61 cm-chord, (d) radiation invariant—all data.

at the flow regimes encountered for an angle  $\alpha_g$  of  $-5^\circ$  and  $5.5^\circ$ , have been deduced from the results of Ref. [18]. Fig. 15(a) compares the two calculated sound contributions with the measured far-field noise at 1.3 m in the mid-span plane. In the TS case ( $-5^\circ$ ), the highly correlated tones amplified by the feed-back loop and similar to the ones of Fig. 8 for the NACA-0012 airfoil, have been removed from the spectrum as they do not correspond to the truly random mechanism addressed in the present study. Only the primary humps in the TS wall-pressure and noise spectra are retained for the analysis, ignoring the tones. At high frequencies, all spectra merge and exhibit a similar decay. Therefore, for the sake of clarity, the spectra for  $\alpha_g = 5.5^\circ$  and  $13^\circ$  have been arbitrarily shifted by  $-10$  and  $-20$  dB, respectively. Consequently, the dB-scale must be considered as relative and devoted to the comparison of the measured and calculated results only. The extended Amiet's model yields good results and Howe's asymptotic model behaves as already mentioned in the case of the flat plate. The very good agreement obtained in the TS case is explained by easier measurements of the relatively large spanwise correlation lengths (around 10 mm for the main hump) over a wide frequency range, with respect to the other two flow regimes. This point stresses that noise predictions crucially depend on the accuracy achievable in the aerodynamic input data.

Fig. 15(b) then compares the two calculated narrow-band noise spectra with the measured far-field noise at 2 m, for the same flow speed of 16 m/s in the mid-span plane of the large nozzle set-up. Again for the sake of clarity and consistency with Fig. 15(a), the spectra for  $\alpha_g = 8^\circ$  and  $15^\circ$  have been arbitrarily shifted by  $-20$  and  $-10$  dB, respectively. Note also that the available experimental frequency range is reduced with respect to Fig. 15(a) because of a higher background noise of the installation. Due to a different flow deflection effect in the larger jet, the flow regime corresponding to a given geometrical angle of attack  $\alpha_g$  is different from what would be encountered in the smaller jet [21]. The angles of attack of  $8^\circ$  and  $15^\circ$  have thus been selected to match the above flow conditions corresponding to the random vortex-shedding regime and the fully turbulent regime, respectively. As shown in Ref. [24], the mean flow is very similar at  $5.5^\circ$  (resp.  $13^\circ$ ) in the small wind tunnel as at  $8^\circ$  (resp.  $15^\circ$ ) in the large one, and the corresponding unsteady wall-pressure fluctuations are very close to each other. The spectra exhibit the same variations over the same frequency range with almost the same levels. Furthermore, the spanwise coherence at the trailing edge for the same flow regime (Fig. 19 in Ref. [24]) also bears strong similarity. Consequently, as expected, very similar far-field noise levels are found in Fig. 15 for the same flow regime in both experiments. Fig. 15(b) also shows a good overall agreement between the predictions and the measurements in the large nozzle set-up. Howe's asymptotic model again overpredicts the low frequencies. Similarly to the case of the flat plate, the leading-edge back-scattering in Amiet's model has a more significant effect at low frequencies below 300 Hz with an additional contribution of 1–2 dB and a smaller contribution at mid-frequencies between 600 and 1500 Hz where it yields a maximum level reduction of 1 dB.

### 5.3. Transfer function invariance

As pointed out in Section 2 and in Ref. [18], the radiation ratio  $A$  should not depend on the flow conditions. This has been checked in a first step by plotting separately the present data for the CD cambered airfoil and the flat plate, in Figs. 16(a) and (b). Each airfoil is investigated for a given flow speed, at different angles of attack indicated on the plots. In Fig. 16(a) for the CD airfoil, open and solid symbols stand for the data measured in the large and small wind tunnels, respectively, at 16 m/s. The data sub-sets collapse reasonably well, accounting for the fact that the nozzle scattering is not corrected for. The same collapse is found in Fig. 16(b) for the flat plate at 20 m/s, over an extended frequency range. The high-frequency peak observed at the  $5^\circ$  angle of attack corresponds to the von Kármán vortex shedding; it must be ignored here. Brook's data for the NACA-0012 at zero angle of attack and the flow speeds 38 and 69 m/s are shown in Fig. 16(c). The non-dimensional ratio  $A$  for the smaller speed has been further multiplied by the amount  $|\mathcal{I}(69)/\mathcal{I}(38)|^2$  according to Eq. (6). The theoretical value of  $A$  is also plotted as a solid line in Figs. 16(a)–(c). The small variations of the function  $\mathcal{I}$  due to the slightly different convection speeds associated with different flow regimes are typically less than half a decibel. Therefore they have been ignored and only an averaged curve has been retained on each plot. This procedure provides another way of comparing the measured and predicted data, in a non-dimensional form.

Finally, all experimental data can be gathered in a single plot, Fig. 16(d), which represents the quantity  $A^* = |A/(c^2 \mathcal{J}^2)|$ . This ratio should be invariant even for different flow speeds and chord lengths, according to the analytical model. Indeed, a good overall collapse is again observed, with discrepancies remaining within a maximum scattering of 10 dB over the whole frequency range. Apart from the aforementioned installation effects, this is possibly attributed to the difficulty of properly measuring the spanwise coherence at all frequencies of interest, due to the limited number of sensors.

## 6. Conclusions

The analytical model of trailing-edge noise presented in part 1 and associated with turbulent boundary-layer flows at any subsonic Mach number over an airfoil has been tested both theoretically and experimentally. First it has been favourably compared with alternative analytical or numerical studies. The present approach based on an iterative Schwarzschild's wave scattering PDE model is equivalent to the Wiener–Hopf technique. Furthermore, the good agreement with accurate numerical simulations around a real, slightly cambered airfoil, suggests that the single-airfoil theory assimilating the airfoil to a flat plate with zero thickness is well suited for fan broadband noise modelling. In a second step, prediction results have been compared with previously reported experimental data and more recent dedicated measurements made in open-jet anechoic wind tunnels. This part involved different airfoil shapes, with moderate camber and variable thickness. The far-field sound directivity has been first assessed irrespective of the flow conditions at single frequencies. The analytical results reproduce the measured directivity patterns fairly well, for coherent sources close to the trailing edge forced by TS waves. Next, the set of far-field broadband noise measurements has been used to check the model in terms of frequency content at a given spatial location. Provided the model is fed with accurate correlation lengths and wall-pressure statistics, it predicts an accurate far-field acoustic pressure. The ratio of the sound pressure PSD to the product of the wall-pressure PSD times the corresponding coherence scale is also found to be nearly independent of the flow regime, as far as pure trailing-edge noise is considered.

The effects of the main parameters in the proposed extension of Amiet's trailing-edge noise model have also been assessed. The finite chord length has an influence mainly at low frequencies and should be even more important at oblique radiation angles off the mid-span plane. An upper limit to the application of low-Mach number models has been determined at a free-stream Mach number of 0.3. Below this value, the errors are less than 1 dB. The finite aspect ratio needs to be accounted for below a typical value of 3. The commonly used large aspect-ratio assumption triggers significant errors for smaller values, which are typically met when a rotating blade is split into strips. As a result, the model can be applied to any blade segment of a fan if the wall-pressure statistical parameters are known, namely the PSD, spanwise coherence and mean convection speed of the pressure field induced by the boundary-layer turbulence.

## Acknowledgements

This work is part of a joint research program between Ecole Centrale de Lyon, Valeo Thermal Systems and CETIAT (Centre d'Etudes Techniques des Industries Aéro-Thermiques).

## Appendix A. Asymptotic analysis

Both Eqs. (2) and (4) can be compared in the limit of very high frequencies, for which the radiation integral involved in Amiet's solution reduces to the main trailing-edge scattering term [8]

$$\mathcal{J} \simeq -\frac{e^{2iC}}{iC} \left\{ (1+i)e^{-2iC} \sqrt{\frac{B}{B-C}} E^*[2(B-C)] - (1+i)E^*[2B] + 1 \right\} \quad (10)$$

with

$$C = \bar{K}_1 - \bar{\mu} \left( \frac{x_1}{S_0} - M_0 \right), \quad B = \bar{K}_1 + \bar{\mu}(1 + M_0)$$

The high-frequency trend for an observer in the mid-span plane follows by making  $kc = 2\beta^2\bar{\mu} \rightarrow \infty$ . According to Ref. [16],

$$E(\xi) = \int_0^\xi \frac{\cos t}{\sqrt{2\pi t}} dt + i \int_0^\xi \frac{\sin t}{\sqrt{2\pi t}} dt = C_2 + iS_2$$

with

$$S_2\left(\frac{\pi}{2}x^2\right) = \frac{1}{2} - f(x)\cos\left(\frac{\pi}{2}x^2\right) - g(x)\sin\left(\frac{\pi}{2}x^2\right)$$

$$C_2\left(\frac{\pi}{2}x^2\right) = \frac{1}{2} + f(x)\sin\left(\frac{\pi}{2}x^2\right) - g(x)\cos\left(\frac{\pi}{2}x^2\right)$$

and, for large values of  $x$ ,

$$f(x) \simeq \frac{1}{\pi x}, \quad g(x) \simeq \frac{1}{\pi^2 x^3}$$

Therefore

$$E(\xi) \simeq \frac{1+i}{2} - \frac{ie^{i\xi}}{\sqrt{2\pi\xi}}$$

and only the constant term needs to be retained. The limit behaviour of the squared radiation integral reads

$$|\mathcal{I}|^2 \simeq \frac{(1+M_0)(1-M_0+M_c)}{\bar{\mu}^2 M_c (1+x_1/S_0)} \left[ \frac{\beta^2}{M_c} + M_0 - \frac{x_1}{S_0} \right]^{-2}$$

Let further transform the expressions using  $S_0 = R_e(1 + M_0 \cos \theta_e)$  and

$$\frac{x_1}{S_0} = \frac{\cos \theta_e + M_0}{1 + M_0 \cos \theta_e}$$

in terms of the emission coordinates ( $R_e, \theta_e$ ), that are defined as the true emission angle and propagating distance with respect to the moving fluid [6,9]. These are related to the reception time coordinates by the transformation formulae

$$\cos \theta = \frac{R_e}{R} (\cos \theta_e + M_0), \quad \frac{R}{R_e} = \sqrt{1 + M_0^2 + 2M_0 \cos \theta_e}$$

When introduced in the expression for the far-field pressure PSD, Eq. (2), this yields the asymptotic result

$$\frac{S_{pp} R_e^2}{L \Pi_0^A} \Big|_{kc \rightarrow \infty} = \frac{M_c}{\pi} \frac{\sin^2 \theta_e / 2}{(1 + M_0 \cos \theta_e) [1 + (M_0 - M_c) \cos \theta_e]^2} \tag{11}$$

This result, first derived by Amiet [6], holds for any subsonic Mach number.

The same change of variables can be made in Howe’s Eq. (4). Though complicated without any further assumption, the result greatly simplifies when all second-order terms in the Mach numbers are neglected. This is justified by the low-Mach number approximation made by Howe [9]. As put in a form comparable to Eq. (11), the result is formally found by Howe as

$$\frac{S_{pp}^H |_{M_0^2 \ll 1} R_e^2}{L \Pi_0^H} = \frac{M_c}{\pi} \frac{\sin^2 \theta_e / 2}{(1 + M_0 \cos \theta_e)} \times \frac{(1 - M_0 + M_c)}{[1 + (M_0 - M_c) \cos \theta_e]^2 [1 + (M_0 - M_w) \cos \theta_e]^2} \tag{12}$$

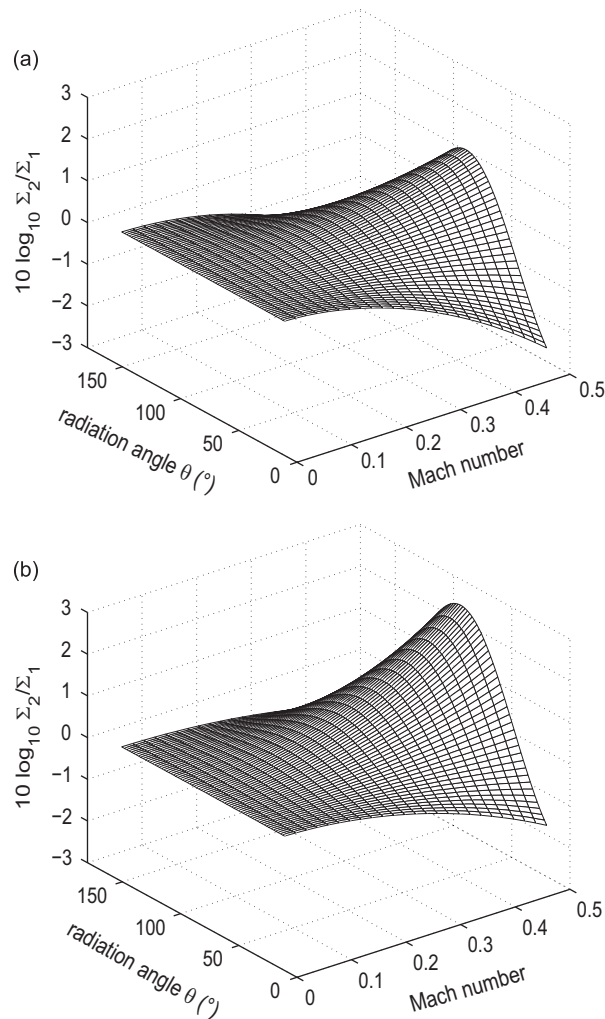


Fig. 17. Ratio of  $\Sigma_2$  and  $\Sigma_1$  functions involved in Howe's transformation from reception to emission coordinates, in decibel scale: (a)  $M_w = 0.5M_0$ , (b)  $M_w = 0$ .

Eqs. (4) and (12) should differ at high subsonic Mach numbers. To get more insight in the approximation, the values of the functions  $\Sigma_1$  and  $\Sigma_2$  defined as

$$\Sigma_1 = \frac{S_{pp}^H}{L\Pi_0^H}, \quad \Sigma_2 = \frac{S_{pp}^H |_{M_0^2 \ll 1}}{L\Pi_0^H}$$

have been computed using Howe's original Eq. (4) and the asymptotic expression (12) to assess the validity of the low-Mach number approximation. Both expressions are compared in Fig. 17, where the ratio  $\Sigma_2/\Sigma_1$  is plotted in decibels as a function of the observation angle and the flow Mach number. The ratio is about 1 at low speeds but significant discrepancies are obtained at high subsonic Mach numbers, with errors of almost 3 dB at  $M_0 = 0.5$ . This suggests that Howe's analysis remains valid up to a Mach number 0.3 with a reasonable accuracy. Amiet's solution, in contrast, has no such limitation with respect to the flow speed.

Another point is that Eqs. (11) and (12) differ by the ratio  $DM_w = [1 + (M_0 - M_w) \cos \theta_e]^2$ , involving the convection speed of the secondary vortices shed in the wake due to the Kutta condition. As already mentioned above, these vortices are explicitly accounted for in Howe's analysis based on a generalised vortex-sound

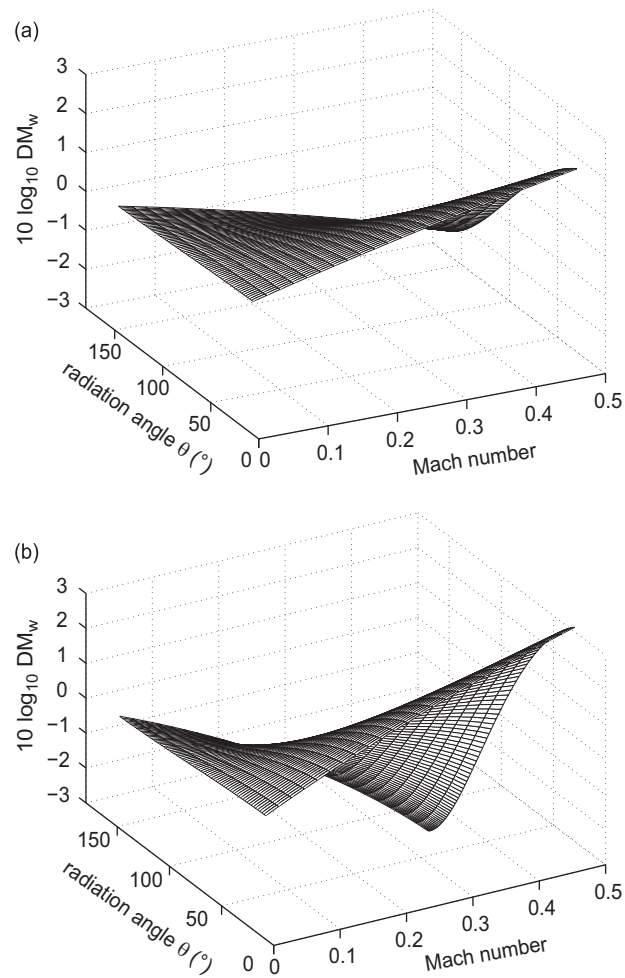


Fig. 18. Ratio  $DM_w = [1 + (M_0 - M_w)\cos\theta_e]^2$  of Amiet's and Howe's high-frequency solutions, in decibel scale: (a)  $M_w = 0.5M_0$ , (b)  $M_w = 0$ .

analogy, in the same way as the incident boundary-layer vortices. They are understood as moving sources. The factor is missing in Amiet's analysis based on the Ffowcs Williams and Hawkins analogy, in which the equivalent sources are unsteady lift forces. These forces are distributed on the airfoil surface and understood as stationary sources. This difference has been already pointed out by Brooks [17], who attributed it to a different modelling of the effect of mean flow on source radiation. For completeness,  $DM_w$  is plotted in Fig. 18, showing typical discrepancies of about 2 dB at a flow Mach number of 0.5 if  $M_w = 0.5M_0$  and twice these values if  $M_w = 0$ . It should be noted that at the flow speeds and the radiation angles reachable in most experiments, close to the normal to the airfoil surface, the discrepancies are much smaller, less than 1 dB. The results suggest that both formulations are comparable at low Mach numbers despite the different problem statements. As a result, asymptotic Howe's formula can be understood as the high-frequency limit of Amiet's formula at low speed. Nevertheless, the relative validity of both formulations with respect to the comparison with dedicated experiments remains an open question, essentially because significant differences are only expected at high speeds.

Independently of the above differences, asymptotic trends for very low-speed flows are derived below, dedicated to fan noise applications with typical Mach numbers around 0.1. For convenience, the results will be expressed in terms of the reception coordinates  $(R, \theta)$ . Dealing first with the dipole directivity factor in Eq. (2),

the result is

$$\left(\frac{x_3}{S_0^2}\right)^2 = \frac{\sin^2\theta_e}{R_e^2(1 + M_0 \cos\theta_e)^4} = \frac{\sin^2\theta}{R^2[\beta^2 + M_0^2 \cos^2\theta]^2} \simeq \frac{\sin^2\theta}{R^2}$$

leading to the classical value for a stationary dipole. This means that the sound can be assessed ignoring the convection by the mean flow, which only holds to the first order in the Mach number and because the dipoles are normal to the flow direction. The simplified Amiet's equation reads

$$S_{pp}^A(\vec{x}, \omega) \simeq \left(\frac{kc}{2\pi}\right)^2 \frac{\sin^2\theta L}{R^2} \frac{1}{2} |\mathcal{S}|^2 \Phi_{pp}(\omega) l_y(\omega) \quad (13)$$

in which  $\mathcal{S}$  includes both the main scattering term and the back-scattering correction.

In the same conditions, Howe's equation in the mid-span plane reduces to the equation

$$S_{pp}^H(\vec{x}, \omega) \simeq \left(\frac{\sqrt{2}}{\pi}\right)^2 \frac{L}{2} \frac{\sin^2(\theta/2) M_c \Phi_{pp}(\omega) l_y(\omega)}{R^2(1 - M_c)[1 + 2(M_0 - M_c - M_w) \cos\theta]} \quad (14)$$

in which the factors in the denominator must be considered to the first order in the Mach number. In practical subsonic situations, only the term  $(1 - M_c)$  plays a significant role, whereas the term  $[1 + 2(M_0 - M_c - M_w) \cos\theta]$  can often be neglected.

## References

- [1] S. Caro, S. Moreau, Aeroacoustic modeling of low pressure axial flow fans, *Sixth AIAA/CEAS Aeroacoustics Conference*, Lahaina, Hawaii, AIAA Paper 2000-2094, July 2000.
- [2] I.J. Sharland, Sources of noise in axial flow fans, *Journal of Sound and Vibration* 1 (3) (1964) 302–322.
- [3] S.E. Wright, The acoustic spectrum of axial flow machines, *Journal of Sound and Vibration* 45 (2) (1976) 165–223.
- [4] M. Roger, S. Moreau, Broadband fan noise prediction using single-airfoil theory—part I: theoretical background, *Fan Noise 2003 International Symposium*, Senlis, France, 2003.
- [5] R.K. Amiet, Noise due to turbulent flow past a trailing edge, *Journal of Sound and Vibration* 47 (3) (1976) 387–393.
- [6] R.K. Amiet, Effect of the incident surface pressure field on noise due to turbulent flow past a trailing edge, *Journal of Sound and Vibration* 57 (2) (1978) 305–306.
- [7] R.K. Amiet, Acoustic radiation from an airfoil in a turbulent flow, *Journal of Sound and Vibration* 41 (4) (1975) 407–420.
- [8] M. Roger, S. Moreau, Back-scattering correction and further extensions of Amiet's trailing edge noise model. Part I: theory, *Journal of Sound and Vibration* 286 (3) (2005) 477–506.
- [9] M.S. Howe, A review of the theory of trailing-edge noise, *Journal of Sound and Vibration* 61 (3) (1978) 437–465.
- [10] M.S. Howe, *Acoustics of Fluid–Structure Interactions*, Cambridge University Press, Cambridge, 1998.
- [11] J.E. Ffowcs Williams, L.H. Hall, Aerodynamic sound generation by turbulent flow in the vicinity of a scattering half-plane, *Journal of Fluid Mechanics* 40 (1970) 657–670.
- [14] M.S. Howe, Edge-source acoustic Green's function for an airfoil of arbitrary chord with application to trailing-edge noise, *The Quarterly Journal of Mechanics and Applied Mathematics* 54 (1) (2001) 139–155.
- [15] T.F. Brooks, T.H. Hodgson, Trailing edge noise prediction from measured surface pressures, *Journal of Sound and Vibration* 78 (1) (1981) 69–117.
- [16] M. Abramowitz, I.A. Stegun, *Handbook of Mathematical Functions*, Dover Publications, New York, 1970.
- [17] T.F. Brooks, Letters to the editor: Trailing-edge noise prediction using Amiet's method, *Journal of Sound and Vibration* 77 (3) (1981) 437–439.
- [18] M. Roger, S. Moreau, Broadband self-noise from loaded fan blades, *AIAA Journal* 42 (3) (2002) 536–544.
- [19] Q. Zhou, P. Joseph, A frequency domain numerical method for airfoil broadband self-noise prediction, *Journal of Sound and Vibration* 299 (2007) 504–519.
- [20] Y. Rozenberg, M. Roger, A. Guédel, S. Moreau, Rotating blade self noise: experimental validation of analytical models, AIAA Paper 2007-3709, May 2007.
- [21] S. Moreau, M. Henner, G. Iaccarino, M. Wang, M. Roger, Analysis of flow conditions in free-jet experiments for studying airfoil self-noise, *AIAA Journal* 41 (10) (2003) 1895–1905.
- [22] R.W. Paterson, R.K. Amiet, Noise of a model helicopter rotor due to ingestion of turbulence, NASA CR-3213, 1979.
- [23] R.H. Schlinker, R.K. Amiet, Helicopter trailing edge noise, NASA CR-3470, 1981.
- [24] S. Moreau, M. Roger, Effect of airfoil aerodynamic loading on trailing edge noise sources, *AIAA Journal* 43 (1) (2003) 41–52.
- [25] M. Roger, S. Moreau, A. Guédel, Vortex-shedding noise and potential-interaction noise modelling by a reversed Sears' problem, AIAA Paper 2006-2607, May 2006.

- [26] S. Pérennès, M. Roger, Aerodynamic noise of a two-dimensional wing with high-lift devices, *Fourth AIAA/CEAS Aeroacoustics Conference*, Toulouse, France, AIAA Paper 98-2338, July 1998.
- [27] S. Pérennès, Caractérisation des Sources de Bruit Aérodynamique à Basses Fréquences de Dispositifs Hypersustentateurs, PhD Thesis No. 99-32, Ecole Centrale de Lyon, 1999.
- [28] B. Noble, *Methods Based on the Wiener–Hopf Technique for the Solution of Partial Differential Equations*, Pergamon Press, New York, 1958 reissued Chelsea Publishing Company, New York, 1988.
- [29] K. Schwartzschild, Die beugung und polarisation des lichts durch einen spalt—i, *Mathematische Annalen* 55 (1902) 177–247.
- [30] M. Landahl, *Unsteady Transonic Flow*, Pergamon Press, New York, 1961.
- [31] A. Oberai, F. Roknaldin, T.J.R. Hughes, Computational procedures for determining structural-acoustic response due to hydrodynamic sources, *Computer Methods in Applied Mechanics and Engineering* 190 (2000) 345–361.
- [32] A. Oberai, F. Roknaldin, T.J.R. Hughes, Computation of trailing edge noise due to turbulent flow over an airfoil, *AIAA Journal* 40 (11) (2002) 2206–2216.
- [33] M. Wang, P. Moin, Computation of trailing-edge flow and noise using large-eddy simulation, *AIAA Journal* 38 (12) (2000) 2201–2209.
- [34] H. Arbey, J. Bataille, Noise generated by airfoil profiles placed in a uniform laminar flow, *Journal of Fluid Mechanics* 134 (1983) 33–47.
- [35] A. McAlpine, E.C. Nash, M.V. Lawson, On the generation of discrete frequency tones by the flow around an aerofoil, *Journal of Sound and Vibration* 222 (5) (1999) 753–779.
- [36] S. Moreau, C. Schram, M. Roger, Diffraction effects on the trailing-edge noise measured in an open-jet anechoic wind tunnel, AIAA Paper 2007-3706, May 2007.
- [37] J.C. Yu, M.C. Joshi, On sound radiation from the trailing edge of an isolated airfoil in a uniform flow, AIAA Paper 79-0603, July 1979.
- [38] W.W. Willmarth, F.W. Roos, Resolution and structure of the wall pressure field beneath a turbulent boundary layer, *Journal of Fluid Mechanics* 22 (1965) 81–94.
- [40] M. Roger, S. Moreau, Fan broadband noise prediction using hybrid methods and analytical modeling, *INTER-NOISE 2006 Conference*, Honolulu, Hawaii, IN06-488 paper, February 2006.
- [41] M. Gaster, The structure and behaviour of laminar separation bubbles, AGARD CP-4, 1966, pp. 813–854.
- [42] S. Moreau, M. Roger, Competing broadband noise mechanisms in low speed axial fans, *AIAA Journal* 45 (1) (2007) 48–57.